Cold-Atom Particle Collider

Guo-Xian Su,[1,2,*,‡] Jesse J. Osborne,[3,‡] and Jad C. Halimeh[4,5,6,7,†]

[1] *Department of Modern Physics, University of Science and Technology of China, Hefei, Anhui 230026, China*
[2] *Physikalisches Institut, Ruprecht-Karls-Universität Heidelberg, Im Neuenheimer Feld 226, Heidelberg 69120, Germany*
[3] *School of Mathematics and Physics, The University of Queensland, St. Lucia, QLD 4072, Australia*
[4] *Max Planck Institute of Quantum Optics, Garching 85748, Germany*
[5] *Department of Physics and Arnold Sommerfeld Center for Theoretical Physics (ASC), Ludwig-Maximilians-Universität München, Theresienstraße 37, München D-80333, Germany*
[6] *Munich Center for Quantum Science and Technology (MCQST), Schellingstraße 4, München D-80799, Germany*
[7] *Dahlem Center for Complex Quantum Systems, Freie Universität Berlin, Berlin 14195, Germany*

(Received 4 March 2024; accepted 30 August 2024; published 22 October 2024)

A major objective of the strong ongoing drive to realize quantum simulators of gauge theories is achieving the capability to probe collider-relevant physics on them. In this regard, a highly pertinent and sought-after application is the controlled collisions of elementary and composite particles, as well as the scattering processes in their wake. Here, we propose particle-collision experiments in a cold-atom quantum simulator for a $1+1$D (one spatial and one temporal dimension) U(1) lattice gauge theory with a tunable topological θ term, where we demonstrate an experimentally feasible protocol to impart momenta to elementary (anti)particles and their meson composites. We numerically benchmark the collisions of moving wave packets for both elementary and composite particles, uncovering a plethora of rich phenomena, such as oscillatory string dynamics in the wake of elementary (anti)particle collisions due to confinement. We also probe string inversion and entropy production processes across Coleman's phase transition through far-from-equilibrium quenches. We further demonstrate how collisions of composite particles unveil their internal structure. Our work paves the way towards the experimental investigation of collision dynamics in state-of-the-art quantum simulators of gauge theories, and sets the stage for microscopic understanding of collider-relevant physics in these platforms.

DOI: 10.1103/PRXQuantum.5.040310

I. INTRODUCTION

Particle collider experiments are key to unlocking the nature of elementary particles and their interactions, and have yielded deep insights into the Standard Model of particle physics [1]. They unravel subatomic structures, enable the discovery of new particles [2,3], and allow the creation of quark-gluon plasmas that mimic the conditions of early universe cosmology [4–6]. Future investment into particle colliders is also taking shape, with the planned high-luminosity upgrade for the Large Hadron Collider and the Future Circular Collider at CERN [7], which will search for physics beyond the Standard Model.

The connection between theoretical predictions and observations in collision experiments currently relies heavily on numerical simulations [12]. Because of the highly nonperturbative and quantum many-body nature of various high-energy scattering events, there is no general *ab initio* method on classical computers that can simulate their real-time collision dynamics from the far-from-equilibrium early stages to late-time equilibration. Traditionally, quantum chromodynamics (QCD) particle collider theory extensively relies on perturbation theory and QCD factorization [1,13,14], but these methods struggle to deal with nonperturbative phenomena such as Schwinger pair production [15] and hadronization [16]. On the other hand, lattice discretization enables nonperturbative numerical simulations for gauge theories; however, among the most prominent classical methods, the highly successful quantum Monte Carlo simulations of lattice QCD suffer from the sign problem in the application to

*Contact author: gxsu@physi.uni-heidelberg.de
†Contact author: jad.halimeh@physik.lmu.de
‡These authors contributed equally to this work.

real-time dynamics. Dedicated time-evolution methods, such as the time-dependent density matrix renormalization group method [17–20], are mostly restricted to spatially (quasi-)one-dimensional systems and to relatively short evolution times due to many-body entanglement buildup, which classical computers fundamentally cannot handle as the computational cost becomes exponential in available resources. As such, phenomenological models have traditionally been employed on classical computers to analyze collider data in order to better understand the underlying highly nonperturbative far-from-equilibrium phenomena [21]. However, these models are not exact, and they rely on various approximations. It is thus useful to seek alternate venues where such collider phenomena can be understood from first-principles time evolution, and where entanglement buildup can be naturally handled.

Inspired by Feynman's vision of simulating the dynamics of a quantum many-body system with an engineered tunable quantum simulator [22–26], the application of quantum simulation to high-energy physics problems has made notable progress over the past years, with experimental demonstrations using trapped-ion platforms, superconducting qubits, and cold-atom quantum gases [27–49]. Such quantum simulators naturally incorporate many-body entanglement by working directly with the wave function, thereby reducing computational complexity in certain cases from exponential to polynomial in the available resources due to quantum advantage. As such, large-scale robust and stabilized quantum simulators of high-energy physics hold the promise to probe nonperturbative far-from-equilibrium collider-relevant physics from first principles, providing temporal snapshots of their microscopic workings [34,37]. Furthermore, high-energy physics is an ideal field for driving progress in quantum simulators, as it offers a myriad of highly nonperturbative far-from-equilibrium quantum processes that are expected to generate a lot of quantum entanglement, such as hadronization, where quantum advantage can prove crucial [16]. This gives rise to a two-way street between high-energy physics and quantum simulation, where the former provides true tests of quantum advantage for the latter, and the latter delivers tangible devices to probe the former.

In recent years, cold-atom quantum simulators have made a significant leap forward towards the simulation of a model of $1+1$D lattice quantum electrodynamics (QED). These include large-scale setups using optical superlattices [8,9,50–52], facilitated by controlled schemes for the stabilization of gauge invariance against errors [53–56], as well as Rydberg-atom arrays [40,57], among many others [34–38]. Remarkably, QED in one spatial dimension serves as a prototype for three-dimensional QCD as they share many intriguing phenomena, from confinement to spontaneous pair production and string breaking. The scattering of excitations in $1+1$D models has attracted much attention in recent years, with numerical studies performed in quantum field theories [58–62] as well as in quantum spin models [63,64]. However, as the methods utilized in those works rely on integrating over momentum eigenstates of excitations, they are not particularly feasible to realize on a tabletop quantum simulator. This is particularly concerning given that it is of strong interest to the community to advance state-of-the-art quantum simulators to the level where they can probe processes mimicking those in particle collision experiments [37], as this will bring these quantum simulators closer to their end goal of becoming complementary venues to particle colliders.

In this work, we propose particle collision experiments in a state-of-the-art optical-superlattice quantum simulator of a U(1) gauge theory, building on the proposal introduced in Refs [8,10]. We introduce an experimentally feasible scheme to impart momenta on elementary and composite particles through holding potential walls, and then propose various collision experiments where rich physics can be probed; see Fig. 1(a). Using numerical methods based on matrix product state (MPS) techniques [19,20,65,66], we show that collisions of a wide range of energy scales can be accessed in our quantum simulator, and they give rise to numerous interesting phenomena, from string dynamics in and out of equilibrium, to entropy production, and to the dynamical formation and breaking down of mesons.

II. LATTICE QED IN A COLD-ATOM QUANTUM SIMULATOR

We consider the canonical $1+1$D lattice QED Hamiltonian [67]

$$\hat{H}_{\mathrm{QED}} = -\frac{\tilde{\kappa}}{2a}\sum_{\ell=1}^{L-1}(\hat{\psi}_\ell^\dagger \hat{U}_{\ell,\ell+1}\hat{\psi}_{\ell+1} + \mathrm{H.c.}) + m\sum_{\ell=1}^{L}(-1)^\ell \hat{\psi}_\ell^\dagger\hat{\psi}_\ell + \frac{a}{2}\sum_{\ell=1}^{L-1}(\hat{E}_{\ell,\ell+1}+\hat{E}_{\mathrm{bg}})^2, \tag{1}$$

employing the "staggered fermion" representation [68] where opposite charges (particles and antiparticles) are placed on alternating sites, represented by the fermionic field operators $\hat{\psi}_\ell, \hat{\psi}_\ell^\dagger$ on site ℓ of a chain with a total of L sites. The first term of Hamiltonian (1) is the kinetic energy of fermionic hopping coupled by the dynamical gauge field $\hat{U}_{\ell,\ell+1}$ on the link between sites ℓ and $\ell+1$, controlled by the lattice spacing a with strength $\tilde{\kappa}$, and the second term is the fermionic occupation with rest mass m. Together, these two terms control the strength of the Schwinger pair production and annihilation process. The last term is the energy of gauge field coupling, where $\hat{E}_{\ell,\ell+1}$ is the electric field on the link between sites ℓ and $\ell+1$, and $\hat{E}_{\mathrm{bg}} = g(\theta-\pi)/(2\pi)$ is an additional

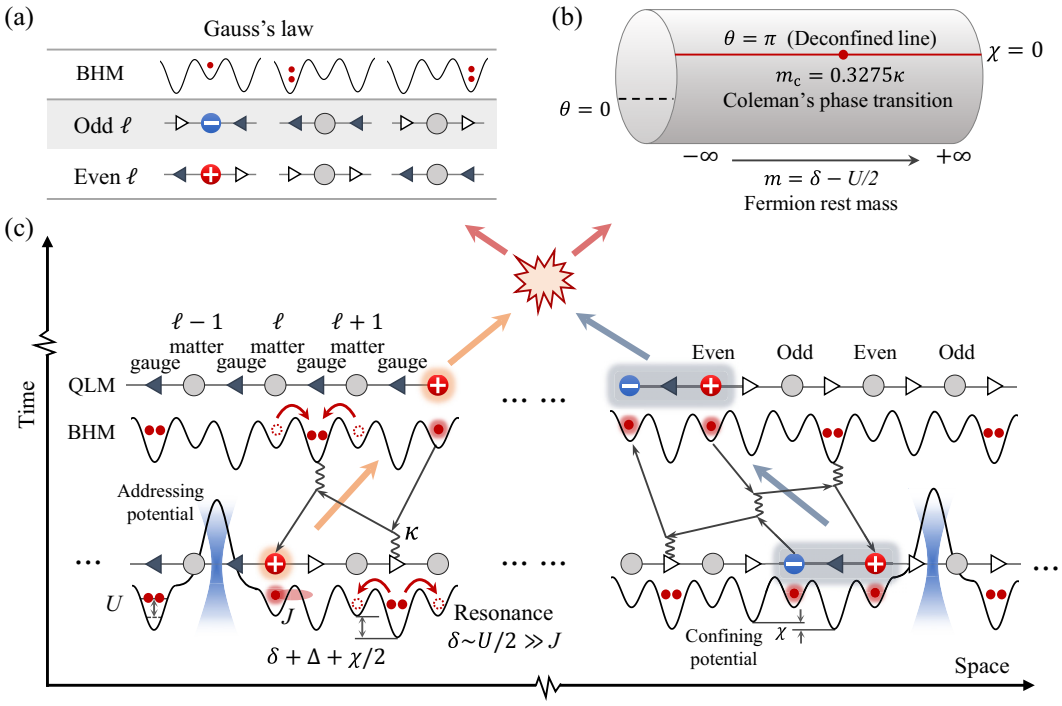

FIG. 1. Schematics of a cold-atom particle collider. (a) Mapping the Bose-Hubbard model onto the quantum link model and Gauss's law [8–10]. Using the staggered-fermion representation, a single atom on an odd (even) matter site represents a particle, denoted as "−" (electron), or an antiparticle, denoted as "+" (positron). The local U(1) gauge symmetry manifests Gauss's law, represented by the configurations shown in the table when working in the physical gauge sector $\hat{G}_\ell|\Psi\rangle = 0$. (b) The θ-m phase diagram of quantum electrodynamics. The staggering potential χ on gauge sites tunes the topological θ angle away from $\theta = \pi$, breaking the degeneracy between the two electric fluxes, which leads to confinement. At $\theta = \pi$, we have Coleman's phase transition at critical mass $m_c = 0.3275\kappa$ [11]. (c) Exploring the scattering process in U(1) lattice gauge theory. In the staggered optical superlattice, the dynamics of atoms can be described by tunneling J, onsite interaction U, a linear tilt Δ, a period-2 staggering δ, and a period-4 staggering χ. The gauge-invariant coupling is realized by the second-order correlated hopping in the BHM, with strength $\kappa \approx 8\sqrt{2}J^2/U$, and the (anti)particle rest mass $m = \delta - U/2$. In the large-mass limit, the hopping of an (anti)particle is a second-order process in gauge theory with strength $\tilde{t} \approx \kappa^2/8m$. To explore particle collisions in the quantum simulator, we prepare the unidirectional moving wave packets of a single (anti)particle or a composite particle (meson) by placing a potential barrier next to the particle, which can be realized in the experiment with a blue-detuned addressing beam.

homogeneous background electric field, where g is the gauge coupling strength and $\theta \in [0, 2\pi)$ is the topological angle. This term tunes a confinement-deconfinement transition [69].

In order to facilitate the numerical simulation and experimental implementation of QED on modern quantum simulators, a so-called quantum link model (QLM) formulation is adopted [70–72], where the dynamical gauge field $\hat{U}_{\ell,\ell+1}$ and electric flux operators $\hat{E}_{\ell,\ell+1}$ are represented by spin operators: $\hat{U}_{\ell,\ell+1} \to \hat{S}^+_{\ell,\ell+1}/\sqrt{S(S+1)}$, $\hat{E}_{\ell,\ell+1} \to g\hat{S}^z_{\ell,\ell+1}$. This representation satisfies the canonical commutation relation $[\hat{E}_{\ell,\ell+1}, \hat{U}_{k,k+1}] = g\delta_{\ell k}\hat{U}_{k,k+1}$, and, in the Kogut-Susskind limit $S \to \infty$, the canonical commutation relation $[\hat{U}_{\ell,\ell+1}, \hat{U}^\dagger_{k,k+1}] = 0$. We further perform the particle-hole transformation [73] for odd sites ℓ: $\hat{\psi}_\ell \to \hat{\psi}^\dagger_\ell$ and $\hat{S}^z_{\ell-1,\ell} \to -\hat{S}^z_{\ell-1,\ell}$; this renders Eq. (1) as

$$\begin{aligned}\hat{H}_{\mathrm{QLM}} = &-\frac{\kappa\sqrt{3}}{4a\sqrt{S(S+1)}}\sum_{\ell=1}^{L-1}(\hat{\psi}_\ell\hat{S}^+_{\ell,\ell+1}\hat{\psi}_{\ell+1} + \mathrm{H.c.}) \\ &+ m\sum_{\ell=1}^{L}\hat{\psi}^\dagger_\ell\hat{\psi}_\ell + \frac{ag^2}{2}\sum_{\ell=1}^{L-1}(\hat{S}^z_{\ell,\ell+1})^2 \\ &- a\chi\sum_{\ell=1}^{L-1}(-1)^\ell\hat{S}^z_{\ell,\ell+1}, \end{aligned} \tag{2}$$

where $\kappa = 2\tilde{\kappa}/\sqrt{3}$ is used to obtain a coupling constant of $\kappa/2$ in the $S = 1/2$ case, which will become convenient when we restrict to $S = 1/2$ later on [in which case, the gauge coupling term $\propto (\hat{S}^z_{\ell,\ell+1})^2$ becomes a constant

energy shift, and so does not have any effect]. The continuum limit of QED is recovered at $S \to \infty$ and $a \to 0$ [74–77]. The last term is a staggering potential on the gauge fields, which realizes the background electric field $\hat{E}_{\rm bg}$ that tunes the topological θ angle in the large-spin limit $S \to \infty$, with $\chi = g^2(\theta - \pi)/(2\pi)$ for half-integer S [10,57,78].

The U(1) gauge transformation is generated by the local Gauss-law operators

$$\hat{G}_\ell = (-1)^\ell [\hat{S}^z_{\ell,\ell+1} + \hat{S}^z_{\ell-1,\ell} + \hat{\psi}^\dagger_\ell \hat{\psi}_\ell], \tag{3}$$

which commute with the QLM Hamiltonian (2): $[\hat{G}_\ell, \hat{H}_{\rm QLM}] = 0$ for all ℓ; this underlines local gauge invariance in that particle hopping must be accompanied by concomitant changes in the local electric fields such as to preserve Gauss's law. As per convention, we choose to work in the *physical* gauge sector of states $|\Psi\rangle$ satisfying $\hat{G}_\ell |\Psi\rangle = 0$ for all ℓ.

Following the experimental realization of the spin-1/2 U(1) QLM in a large-scale Bose-Hubbard quantum simulator [8,9,50–52], we henceforth restrict to this case in which $S = 1/2$. The local electric field spans the basis $\{|\blacktriangleleft\rangle, |\triangleright\rangle\}$ encoding two eigenstates of the spin-1/2 operator $\hat{S}^z_{\ell,\ell+1}$; see Fig. 1(b). The gauge coupling term $\propto (\hat{S}^z_{\ell,\ell+1})^2 = \mathbb{1}_{\ell,\ell+1}/4$ becomes an inconsequential constant energy term that does not contribute to the dynamics at $S = 1/2$. The spin-1/2 U(1) QLM is deconfined at $\theta = \pi$ and hosts Coleman's phase transition at the critical mass $m_{\rm c} = 0.3275(15)\kappa$ [11,79], which is related to the spontaneous breaking of a global $\mathbb{Z}_2$ symmetry connected to charge conjugation and parity symmetry conservation; see Fig. 1(c). For $m \to +\infty$, the ground-state manifold of $\hat{H}_{\rm QLM}$ corresponds to the two degenerate vacua $|\ldots, \blacktriangleleft, \varnothing, \blacktriangleleft, \varnothing, \blacktriangleleft, \ldots\rangle$ and $|\ldots, \triangleright, \varnothing, \triangleright, \varnothing, \triangleright, \ldots\rangle$, where $\varnothing$ represents the absence of matter at a site. In this case ($\theta = \pi$), no string tension is present between a particle-antiparticle pair. Tuning the θ angle away from π creates an additional background electric field $\hat{E}_{\rm bg}$ that explicitly breaks this global $\mathbb{Z}_2$ symmetry, creating an energy difference between the two electric fluxes $\{|\blacktriangleleft\rangle, |\triangleright\rangle\}$. As a result, a particle-antiparticle pair connected by a string of D electric fluxes $|\blacktriangleleft\rangle$ experiences the string energy χD that increases linearly with D. Subsequently, the spin-1/2 QLM becomes a confining theory. A particle-antiparticle pair in the confined $1+1$D QED theory forms a two-particle bound state, analogous to a meson in $3+1$D QCD, which is a composite particle made of a quark-antiquark pair formed by the gluon flux tube connecting them [69,80].

The quantum simulator used to experimentally realize the spin-1/2 QLM is governed by the Bose-Hubbard model (BHM) Hamiltonian [8]

$$\hat{H}_{\rm BHM} = -J \sum_{j=1}^{N-1} (\hat{b}^\dagger_j \hat{b}_{j+1} + \hat{b}^\dagger_{j+1} \hat{b}_j) + \frac{U}{2} \sum_{j=1}^{N} \hat{n}_j (\hat{n}_j - 1) + \sum_{j=1}^{N} \mu_j \hat{n}_j \tag{4}$$

with $\hat{b}_j$, $\hat{b}^\dagger_j$ the bosonic field operators, J the tunneling strength between neighboring sites, U the on-site interaction, and $N = 2L$ the total number of sites in the quantum simulator. The chemical potential term is used to engineer the correlated hopping process that implements the gauge theory Hamiltonian (2) at $S = 1/2$. It takes the form $\mu_j = j\,\Delta + (-1)^j \delta/2 + \sin(j\pi/2)\chi/2$, where Δ is a linear tilt used to suppress long-range single-atom tunneling [81], and δ is a staggering potential generated by a period-2 optical superlattice separating the system into two sublattices, with the even sites denoted as "matter" $j_{\rm M} \to \ell$ (for even j) and the odd sites denoted as "gauge" $j_{\rm G} \to (\ell, \ell+1)$ (for odd j). For $\delta \sim U/2 \gg J$, we identify the resonant second-order correlated hopping process $-(\kappa/2\sqrt{2})[\hat{b}_{j-1}(\hat{b}^\dagger_j)^2 \hat{b}_{j-1} + \text{H.c.}]$ (with odd j) where single bosons on neighboring matter sites annihilate (create) to form a doublon (hole) on the gauge site in between; see Fig. 1(a). As a result, the Bose-Hubbard model realizes the quantum link model Hamiltonian (2), and we identify $\kappa \approx 8\sqrt{2}J^2/U$ and $m = \delta/2 - U$ by using second-order perturbation theory [8]. The confining term $\propto \chi$ is a staggered potential on gauge sites generated by a period-4 optical superlattice [10], which breaks the degeneracy between the two vacua $|\ldots, \blacktriangleleft, \varnothing, \blacktriangleleft, \varnothing, \blacktriangleleft, \varnothing, \blacktriangleleft, \ldots\rangle \leftrightarrow |\ldots, 2, 0, 0, 0, 2, 0, 0, \ldots\rangle$ and $|\ldots, \triangleright, \varnothing, \triangleright, \varnothing, \triangleright, \varnothing, \triangleright, \ldots\rangle \leftrightarrow |\ldots, 0, 0, 2, 0, 0, 0, 2, \ldots\rangle$, where here we show their bosonic representation on the optical superlattice.

For all numerical simulations we have performed in this paper, we use the experimentally tested parameters $J = 58$ Hz, $U = 1368$ Hz, $\Delta = 57$ Hz [9], and subsequently $\kappa \approx 28$ Hz. In order to simulate a desired mass m, we tune the value of δ in order to satisfy the above-stated relation $m = \delta/2 - U$.

III. COLD-ATOM "PARTICLE ACCELERATOR"

The basic ingredients of particle collision experiments are the spatially localized moving wave packets of elementary or composite particles [82]. An elementary particle or antiparticle excitation in the vacuum background can be expressed as $|\ldots, \triangleright, \varnothing, \triangleright, -, \blacktriangleleft, \varnothing, \blacktriangleleft, \ldots\rangle$ or $|\ldots, \blacktriangleleft, \varnothing, \blacktriangleleft, +, \triangleright, \varnothing, \triangleright, \ldots\rangle$, which corresponds to the state $|\ldots, 2, 0, 0, \mathit{1}, 0, 0, 2, \ldots\rangle$ in the Bose-Hubbard model (a single boson $|\mathit{1}\rangle$ on an odd matter site for a particle and an even matter site for an antiparticle); see also Fig. 1(b). A particle-antiparticle meson excitation

$|\ldots, \triangleright, \varnothing, \triangleright, -, \blacktriangleleft, +, \triangleright, \varnothing, \triangleright, \ldots\rangle$ corresponds to the state $|\ldots, 2, 0, 0, \mathit{1,0,1}, 0, 0, 2, \ldots\rangle$.

We first consider the regime $m \gg m_c$ where the rest mass dominates, and spontaneous Schwinger pair production is exponentially suppressed. The (anti)particle hopping is a second-order process in the QLM with a virtual pair creation as an intermediate step; see Fig. 1(a) and Appendix A. Therefore, the low-energy effective Hamiltonian of the quantum link model (2) becomes

$$\hat{H}_{(\mathrm{A})\mathrm{P}} = -\tilde{t} \sum_{\ell_{(\mathrm{A})\mathrm{P}}} (\hat{\psi}^{\dagger}_{\ell_{(\mathrm{A})\mathrm{P}}} \hat{\psi}_{\ell_{(\mathrm{A})\mathrm{P}}+1} + \mathrm{H.c.}) + (-1)^{\sigma_{(\mathrm{A})\mathrm{P}}} 2\chi \sum_{\ell_{(\mathrm{A})\mathrm{P}}} \ell_{(\mathrm{A})\mathrm{P}} \hat{\psi}^{\dagger}_{\ell_{(\mathrm{A})\mathrm{P}}} \hat{\psi}_{\ell_{(\mathrm{A})\mathrm{P}}}, \quad (5)$$

where $\hat{\psi}_{\ell_{(\mathrm{A})\mathrm{P}}}, \hat{\psi}^{\dagger}_{\ell_{(\mathrm{A})\mathrm{P}}}$ are fermionic fields on (anti)particle sublattice sites (ℓ_{P} for odd ℓ, ℓ_{A} for even ℓ). The background electric field created by the confining potential χ can be understood as an effective linear tilt, with $\sigma_{\mathrm{A}} = 0$ and $\sigma_{\mathrm{P}} = 1$, which makes the tilt positive for the antiparticle and negative for the particle. We identify this effective (anti)particle tunneling strength to be $\tilde{t} = \kappa^2/(8ma^2)$ by using second-order perturbation theory (Appendix A).

A. Single-particle quantum walk

Before we create moving wave packets, we first look at the dynamics of a single particle localized on a lattice site, which is a coherent superposition of all momentum eigenstates within the first Brillouin zone. The localized wave packet has an equal probability of tunneling in both directions. At $\chi = 0$, a single (anti)particle undergoes a quantum walk, analogous to a free electron in a homogeneous lattice [83]. The result is a light-cone-shaped transport, and the wave packet delocalizes, as shown in Fig. 2(a).

To characterize the quantum walk, we numerically calculate the expectation value of the charge density operator in the Bose-Hubbard quantum simulator,

$$\langle \hat{Q}_{j_{\mathrm{M}}}(t)\rangle = \langle \hat{Q}_{\ell}(t)\rangle = \langle \Psi(t)|\, \hat{Q}_{\ell}\, |\Psi(t)\rangle \quad (6)$$

with $|\Psi(t)\rangle = \exp(-i\hat{H}_{\mathrm{BHM}}t)\,|\Psi_0\rangle$ and $\hat{Q}_{\ell} = (-1)^{\ell}\hat{\psi}^{\dagger}_{\ell}\hat{\psi}_{\ell}$, where $|\Psi_0\rangle$ is the initial state and t is the evolution time. We choose $m = 1.5\kappa$ for the numerical simulations as it is large enough to suppress spontaneous pair creation and maintain the mapping to the effective Hamiltonian (5) while keeping the dynamics fast enough for experimental implementations with limited coherence time.

For a single particle, the charge density wavefront on the particle sublattice can be characterized by the Bessel function of the first kind $\mathcal{J}_{\ell_{\mathrm{P}}}$ [84]:

$$|\langle \hat{Q}(t)\rangle|_{\ell_{\mathrm{P}}} = A_0 |\mathcal{J}_{\ell_{\mathrm{P}}}(2 \times 2\pi\tilde{t} \times t)|^2 + B_0. \quad (7)$$

The first-order dynamics of spontaneous pair production and annihilation in the QLM, as well as the direct tunneling

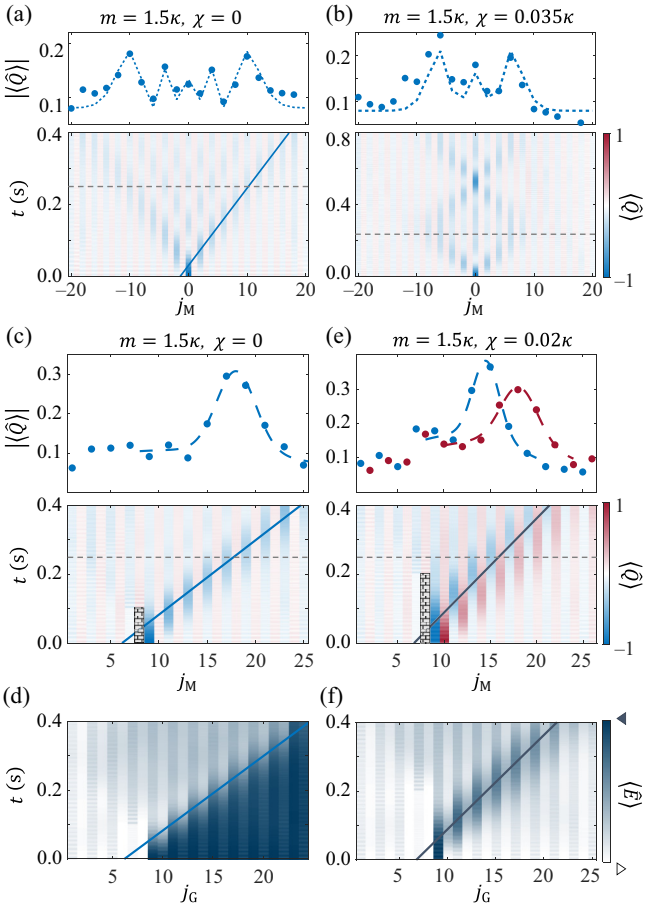

FIG. 2. Single-particle quantum walk and momentum initialization. (a) Single-particle quantum walk on matter sites. The upper panel shows the wavefront at $t = 0.25$ s (gray dashed line in the lower panel), and fitted to the Bessel function (7) (blue dashed line) where $\tilde{t}_{\mathrm{fit}} = 2.1(1)$ Hz, close to $\tilde{t} = 2.33$ Hz predicted by second-order perturbation theory. The propagation speed of the wavefront is 46(2) sites/s, extracted by a linear fit (blue line). (b) Bloch oscillation of a single particle. The wavefront at $t = 0.25$ s (gray dashed line in the lower panel) is fitted to Eq. (8) (blue dashed line) with $\chi_{\mathrm{fit}} = 0.96(2)$ Hz $\approx 0.035\kappa$. (c) The moving wave packet of a single particle created by reflection on the barrier and propagating to the right. The group velocity initiated is $v_{\mathrm{g}}^{(i)} = 47.9(8)$ sites/s (blue line). The upper panel shows the profile of the charge density $|\hat{Q}|$ at $t = 0.25$ s (gray dashed line in the lower panel), which can be fitted by a Gaussian function with width $\sigma \approx 2$ (blue dashed line). (d) The electric flux $\langle\hat{E}\rangle$ changes according to Gauss's law as the particle propagates. (e),(f) A moving meson wave packet consists of a particle (blue) and an antiparticle (red). The group velocity is fitted to be 37.4(4) sites/s (dark blue line).

in the BHM, result in a shift in the background and the reduction of amplitude, which we account for by adding two extra parameters A_0 and B_0. The effective tunneling is fitted to be $\tilde{t}_{\rm fit} = 2.1(1)$ Hz; see the dashed curve in Fig. 2(a). The fitting result is slightly smaller than $\tilde{t} = 2.33$ Hz predicted by the approximate second-order perturbation theory, as the actual dispersion relation deviates slightly from the sinusoidal function expected from the effective model in Eq. (5). This is mainly due to the first-order pair-creation dynamics in the QLM, and thus the actual dispersion is slightly different from the sinusoidal dispersion expected from Eq. (5) [see also Fig. 12(a) in Appendix C]. The propagation speed of the outer wavefront is fitted to be 46(2) sites/s, while the maximum group velocity estimated from the ground band of the effective model is $v_{\rm g}^{\rm max} = 58.6$ sites/s, in particular Eq. (A8). In fact, the group velocity fit 46(2) sites/s actually matches pretty closely to the maximum group velocity from the MPS calculation in Fig. 12(b), $v_{\rm g}^{\rm MPS} = 48.3$ sites/s; see Appendix A.

For $\chi \neq 0$, although there is an external force acting on the (anti)particle, a net transport in the lattice is not possible, as the maximum kinetic energy of the particle is limited by the bandwidth. As a result, the (anti)particle undergoes Bloch oscillations, as shown in Fig. 2(b). In this case, the charge density can be characterized by modifying the argument of the Bessel function [84] as

$$|\langle\hat{Q}(t)\rangle|_{\ell_{\rm P}} = A_0\left|\mathcal{J}_{\ell_{\rm P}}\left[\frac{4\tilde{t}}{2\chi}\sin(2\chi\pi t)\right]\right|^2 + B_0. \quad (8)$$

The dashed line in Fig. 2(b) is a fit to Eq. (8), where we find that $\chi_{\rm fit} = 0.96(2)$ Hz, which agrees well with $\chi = 0.035\kappa = 0.98$ Hz. We notice an imbalance of the wavefront related to the sign of χ, which we attribute to higher-order processes that are not captured by the effective model.

B. Momentum initialization

To explore collision dynamics, previous theoretical works have typically generated unidirectional moving wave packets by numerically building a superposition of momentum eigenstates [59,63,64]. Although this method is straightforward in numerical simulations, it is quite challenging in a cold-atom experiment. Here, we demonstrate a simple scheme to experimentally prepare such moving wave packets with a potential barrier, as illustrated schematically in Fig. 1(a). The potential barrier can be achieved by single-site addressing with a blue-detuned light potential through the high-resolution objective in a quantum gas microscope experiment [52,85,86]. Initially, the momentum superposition of a localized (anti)particle wave packet is centered at zero quasimomentum, $q = 0$. The barrier placed left (right) of the original wave packet reflects the left- (right-)moving momentum components to the right (left), thus shifting the center of the momentum superposition to a finite value, effectively creating a moving wave packet. We show that this method can work for elementary particles in Figs. 2(c) and 2(d) as well as composite particles (mesons) in Figs. 2(e) and 2(f).

We note that, unlike a free-electron theory, here the particle hopping is coupled by the gauge fields, with corresponding flips of electric fluxes as the particle moves, such that Gauss's law (3) is always satisfied; see Fig. 2(d). In our numerical simulations, the barrier is encoded as a local chemical potential placed on the two sites left of the particle with $\mu_{\rm address} = 10\kappa \approx 120\tilde{t}$ large enough to suppress the effective hopping. We remove the barrier at 0.1 s, after the wave packet has moved away. We perform a linear fit of the particle trajectory and find the initial group velocity to be $v_{\rm P}^{\rm (i)} = 47.9(8)$ sites/s, almost identical to the maximum group velocity obtained by the MPS calculation in Appendix A.

For a meson state, pair hopping is a fourth-order process, illustrated on the right of Fig. 1(a). The barrier placed to the right of the particle-antiparticle pair reflects right-moving momentum components, while allowing the particle to hop left, and then the antiparticle follows afterward. In the presence of the confining potential, the external force exerted by the background electric field on the particle is $F_{\rm P} \propto \chi$ pointing towards the right, and for the antiparticle, it is $F_{\rm A} \propto -\chi$ pointing toward the left. Therefore, no net force is exerted on the center of mass of the pair. However, the same background field creates a string energy proportional to the interparticle distance D. Subsequently, the hopping of the particle increases the string energy, making it energetically favorable for the antiparticle to follow. As a result, the particle-antiparticle pair moves together as a composite particle. We show the case in which $m = 1.5\kappa$ and $\chi = 0.02\kappa$ in Figs. 2(e) and 2(f). We perform a linear fit and find the group velocity of the meson to be $v_{\rm g}^{\rm M} = 37.4(4)$ sites/s. To benchmark the speed of the meson, we calculate the meson band structure using the MPS excitation ansatz (Fig. 11 below; see Appendix C 2 for details). From the ground band dispersion, we find that the maximum group velocity of a meson is about 40 sites/s, which agrees well with the extracted group velocity.

C. Particle acceleration

The most essential feature of a real particle collider is the ability to accelerate the particles close to the speed of light, so that the collision creates a far-from-equilibrium system with such a high energy density that spontaneous particle production becomes possible. To explore the relevant physics in this high energy scale, we investigate particle acceleration in our quantum simulator.

In analogy to conventional particle accelerators, we could imagine imparting energy into our particles by

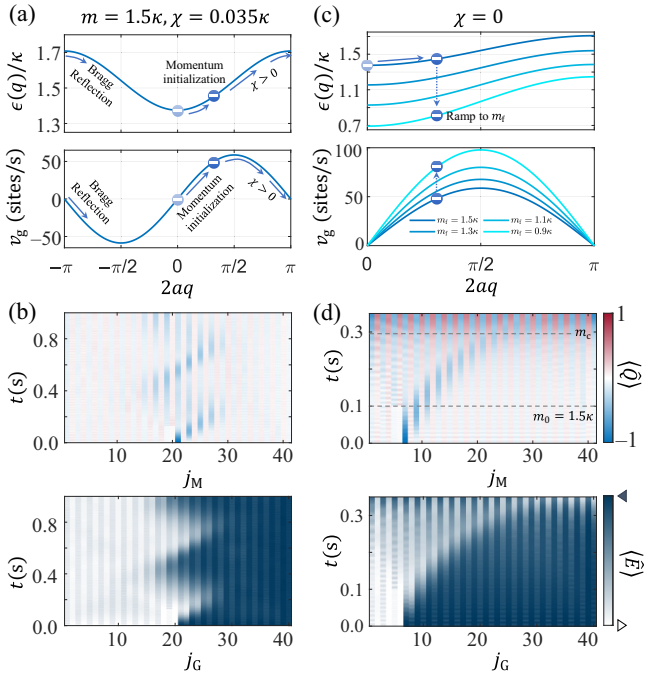

FIG. 3. Real-space Bloch oscillation and particle acceleration. (a) Upper panel: ground band dispersion relation of a single particle [Eq. (A7)]. Lower panel: group velocity calculated from the dispersion [Eq. (A8)]. Although the quasimomentum increases linearly due to the external force induced by χ, the maximum group velocity is bounded by the bandwidth, and the wave packet undergoes Bloch oscillation. (b) Real-space Bloch oscillation of a single-particle moving wave packet. (c) Ground band dispersion of a single particle for different masses [Eq. (A7)]. The group velocity is inversely proportional to the rest mass. (d) Particle acceleration by tuning the rest mass. We prepare the moving wave packet from 0 to 0.1 s at $m = 1.5\kappa$, and starting at 0.1 s, we linearly ramp down the mass to $m = 0$ in 0.25 s. Before reaching the critical point $m_c = 0.3275\kappa$, we find that the particle undergoes continuous acceleration. Below the critical point, we can no longer identify the moving wave packet due to spontaneous particle creation in the vacuum background.

means of an electromagnetic field, which we could implement naively by using the background potential χ. While this would be achievable in the continuum limit, on a lattice, the particles will eventually undergo Bloch oscillations [64]; see Figs. 3(a) and 3(b).

However, unlike a conventional accelerator, we can make use of the tunability of the quantum simulator to directly adjust the value of the rest mass, which, in effect, causes the particles to accelerate. For $m \gg m_c$, the effective tunneling is inversely proportional to the mass m, $\tilde{t} \propto m^{-1}$, and subsequently the group velocity $v_g \propto m^{-1}$ (the quasimomentum of the wave packet remains constant during time evolution for $\chi = 0$); see Fig. 3(c). Moreover, the tunable energy scale between the rest mass and the kinetic energy makes it possible to access regimes where spontaneous pair production dominates the dynamics.

After momentum initialization at a constant mass $m_0 = 1.5\kappa$ from 0 to 0.1 s, we ramp down the mass from m_0 to 0 in 0.25 s, and observe a continuous acceleration of the particle before reaching the critical mass m_c of Coleman's phase transition; see Fig. 3(d). As the critical point is approached, we find that particle-antiparticle pair production in the vacuum background dominates and the initial wave packet is no longer observable.

To benchmark the acceleration, after ramping down the mass to a final mass m_f, we keep the rest mass constant at m_f and let the wave packet propagate at constant velocity starting at t_0; see Fig. 4(a). We extract the position of the wave packet every 0.003s by Gaussian fits and then perform a linear fit to find the group velocity; see Fig. 4(b). As expected from the band structure, the group velocity v_g rises linearly with m_f^{-1} for $m_f \gtrsim \kappa$, and deviates from the linear relationship approaching the critical mass m_c; see Fig. 4(d). By rescaling the evolution time of each curve with its final mass m_f^{-1}, we also find that all the trajectories collapse onto a single line, while small deviations can be found for $m_f \sim m_c$; see Fig. 4(c).

A more interesting protocol of acceleration is instantaneously quenching the mass to m_f at $t = t_0$, which is a global quench that brings the system out of equilibrium [9]; see Figs. 4(e)–4(h). For less violent quenches ($m_f \gtrsim \kappa$), we find that the group velocity maintains $v_g \propto m_f^{-1}$, but deviates from the linear relationship faster than the ramping protocol when approaching m_c. This is expected, since the quench creates more particle-antiparticle excitations in the vacuum background than the ramp. In this case, the wave packets can no longer be extracted below $m_f = 0.3275\kappa$ [$m_f^{-1} m_0 = 4.58$ in Fig. 4(h)].

D. Initial state preparation

Here we describe how these elementary particles and particle-antiparticle pairs can be prepared in a cold-atom quantum simulator. We consider the well-tested experiment with ^{87}Rb atoms in optical superlattices [8]. The proposed experiment starts with a $\langle \hat{n} \rangle = 1$ Mott insulator state, where all atoms are prepared in the hyperfine state $|\downarrow\rangle = |F = 1, m_F = -1\rangle$; see Fig. 5(a). To prepare a single particle excitation, we first address a single atom with a σ^--polarized optical tweezer at a wavelength of 787.55 nm, which creates a light shift acting only on internal state $|\uparrow\rangle = |F = 2, m_F = -2\rangle$ [52,85]. The addressed atoms can then be flipped to $|\uparrow\rangle$ with a resonant microwave field. While this atom is pinned by the addressing beam, we merge the remaining atoms into odd sites with a superlattice [87], creating the state $|\ldots, 2, 0, 1, 1, 2, 0, 2, 0, \ldots\rangle$. We now project σ^- tweezers onto the single atoms along with alternating doublons on every four sites, and flip them to $|\uparrow\rangle$, which are removed by a resonant laser. The resulting state is a single (anti)particle in the vacuum background $|\ldots, 2, 0, 0, 1, 0, 0, 2, 0, \ldots\rangle$.

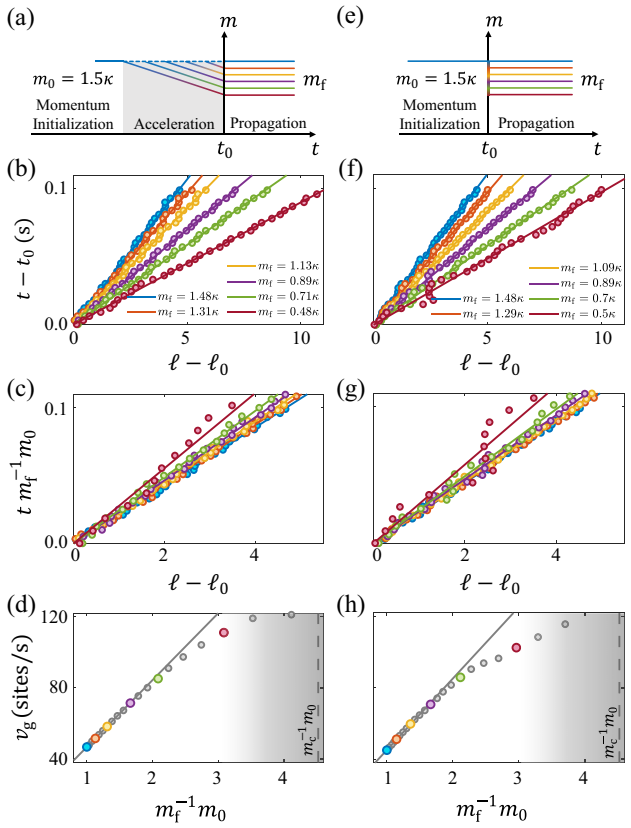

FIG. 4. Analysis of the particle acceleration. (a) Particle acceleration by the ramping mass. After preparing the moving wave packet at $m_0 = 1.5\kappa$ in 0.1 s, we linearly ramp down the mass to m_f and let the wave packet propagate at the final mass. (b) During the propagation, we perform a Gaussian fit for every 0.003 s to extract the position of the moving wave packet, and then obtain the group velocity by fitting the positions. (c) By rescaling the propagation time with m_f, the space-time trajectories of wave packets with different final masses collapse on top of each other. (d) Group velocity is inversely proportional to the final mass, $v_g \propto m_f^{-1}$, for $m_f \gg m_c$, and deviates from the linear relationship when approaching the critical mass m_c. (e) Particle acceleration by quenching the mass from $m_0 = 1.5\kappa$ to m_f at $t = 0$. (f)–(h) Same as (b)–(d). With the quench protocol, the group velocity still follows the linear relationship for larger m_f. However, when approaching m_c, the deviation is faster than the ramping protocol, as the quench creates more particle excitations in the vacuum background.

To prepare a particle-antiparticle pair, we first create a $\mathbb{Z}_2$-ordered product state $|\ldots, 2, 0, 2, 0, \ldots\rangle$ from the $\langle \hat{n} \rangle = 1$ Mott insulator with the superlattice; see Fig. 5(b). By addressing and removing alternating doublons with an array of σ^- tweezers, we create a $\mathbb{Z}_4$-ordered state $|\ldots, 2, 0, 0, 0, 2, 0, 0, 0, \ldots\rangle$ corresponding to a vacuum state in the gauge theory. We now address a single doublon with the σ^- tweezer beam and flip both atoms to the $|\uparrow\rangle$ state; the local chemical potential μ_{address} created by the tweezer tunes the rest mass locally. By tuning the intensity

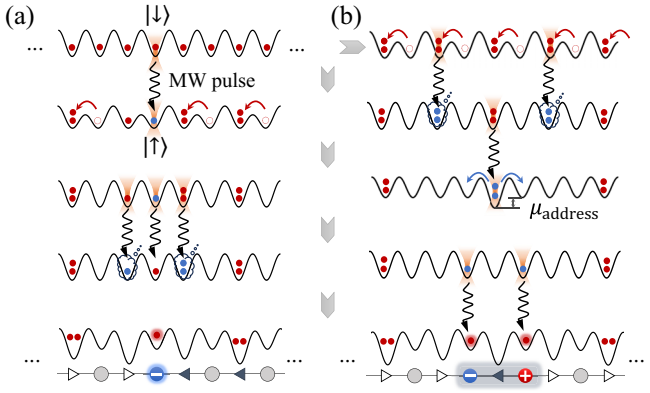

FIG. 5. Initial state preparation and momentum initialization. Red dots denote atoms in the hyperfine state $|\downarrow\rangle = |F = 1, m_F = -1\rangle$, while blue dots denotes atoms in $|\uparrow\rangle = |F = 2, m_F = -2\rangle$. Addressing tweezer beams induce a local ac-Stark shift on the $|\uparrow\rangle$ state, such that the addressed atoms can be individually transferred between $|\downarrow\rangle$ and $|\uparrow\rangle$ with a microwave (MW) pulse. (a) Preparation of a single (anti)particle initial state. (b) Preparation of a particle-antiparticle pair.

of this addressing tweezer we can tune the local rest mass m_{address} to 0 and initiate the second-order correlated tunneling $|0, 2, 0\rangle \to |1, 0, 1\rangle$ to split this doublon into a pair of single atoms on neighboring matter sites, corresponding to a local particle-antiparticle pair in the gauge theory.

IV. COLLISION DYNAMICS

In this section, we demonstrate the rich physics that can be probed with particle collisions in the quantum simulator.

A. Particle-antiparticle collision

We first consider the low-energy collision between a particle and an antiparticle; see Fig. 6(a). The wave packets are initiated to move towards each other, and we probe their collision dynamics by the charge density $\langle \hat{Q} \rangle$ and electric flux $\langle \hat{E} \rangle$. In the large-mass limit ($m \gtrsim \kappa$), spontaneous pair creation and annihilation are suppressed, and the dynamics of (anti)particles follows Hamiltonian (5). Consequently, it is energetically unfavorable for the particle and the antiparticle to annihilate each other and the resulting collision is elastic. We first show this elastic collision for the nonconfining case; see Figs. 6(b)–6(d). The particle and antiparticle undergo a head-on collision from 0.1 to 0.2 s, and subsequently recoil in opposite directions at constant velocities. With linear fits, we find the postcollision velocities to be $v_P^{(f)} = -47.4(5)$ sites/s and $v_A^{(f)} = 48(1)$ sites/s for the particle and antiparticle, respectively. Compared to the group velocity initiated in Fig. 2(b), we find that $v_P^{(f)} = v_A^{(i)}$ and $v_A^{(f)} = v_P^{(i)}$. Since the particle and the antiparticle are identical in mass, this indicates that

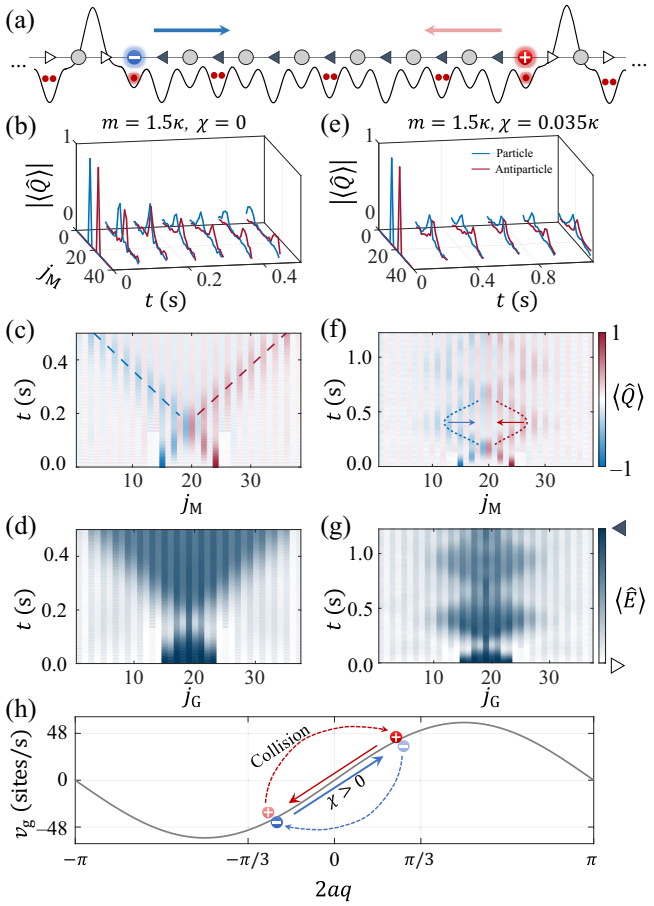

FIG. 6. Particle-antiparticle collisions in the large-mass limit. (a) A schematic illustration of particle-antiparticle collision in the quantum simulator. (b),(e) Expectation value of the charge density $\langle\hat{Q}\rangle$ illustrating the collision of moving particle (blue) and antiparticle (red) wave packets. (c),(f) Same data as in (b) and (e). (d),(g) Expectation value of the electric flux $\langle\hat{E}\rangle$. (b)–(d) Collision dynamics in the deconfined case ($\chi = 0$). After the collision, the final group velocities of the particle and antiparticle are fitted to be $v_P^{(f)} = -47.4(5)$ sites/s (dashed blue line) and $v_A^{(f)} = 48(1)$ sites/s (dashed red line), respectively, indicating an elastic collision. (e)–(g) Collision dynamics in the confined case ($\chi = 0.035\kappa$), where the electric flux $|\blacktriangleleft\rangle$ has higher energy, and the resulting string tension between the particle-antiparticle pair leads to multiple collisions. (h) Illustration of collision dynamics in momentum space. The particle and antiparticle exchange momentum after the collision and move apart in opposite directions. When $\chi > 0$, they are accelerated toward each other by the string tension.

they exchange momenta during an elastic collision; see Fig. 6(h).

In the confined case with positive χ, the electric flux $|\blacktriangleleft\rangle$ has higher energy than $|\triangleright\rangle$, creating a confining force that accelerates the particle and the antiparticle towards each other. We keep the value of χ small to minimize the lattice effect (i.e., the Bloch oscillations) and therefore work within the regime of the positive effective mass ($2aq \in [-\pi/2, \pi/2]$). After the collision, the particle and antiparticle exchange momentum and recoil away from each other. The string energy increases with the interparticle distance D as they move apart, which causes deceleration of the particle and antiparticle. After reaching zero velocity, they start accelerating toward each other again, leading to the next collision. The string dynamics form a particle-antiparticle bound state oscillating dynamically in the vacuum background; see Figs. 6(e)–6(g).

Moving on from the previous low-energy particle collisions, we bring the system out of equilibrium by an abrupt global quench of the rest mass from $m_0 = 1.5\kappa$ to m_f at $t = 0.1$ s, and thus access collision dynamics on a higher energy scale [9,51,88].

The vacuum background itself is unstable under the violent quenches of m [9,57]. Around $m_f = 0$, the vacuum background undergoes persistent oscillation between the two degenerate vacua, being an instance of quantum many-body scarring dynamics that deters the growth of entanglement entropy, which has been established to appear in the QLM by Refs [50,57,89,90]. Approaching the critical mass $m_f \sim m_c$, the scarring dynamics goes away and the vacuum background thermalizes with entanglement entropy maximized. When the mass increases further to $m_f \gg m_c$, the pure vacuum background is close to the ground state of the quantum link model (2), and entropy growth is therefore suppressed again [88].

For $m_f \lesssim m_c$, the particle production in the vacuum background makes it difficult to distinguish the initial colliding particle-antiparticle pair; see Fig. 13 in Appendix D. To better demonstrate the collision dynamics, we subtract the evolution of the vacuum background (Fig. 14 in Appendix D) from the evolution of the particle-antiparticle collision (Fig. 13) for the same quench parameters, and in Fig. 7 we show their difference in charge density $\Delta\hat{Q} = \hat{Q}_{\text{pair}} - \hat{Q}_{\text{vac}}$ and the bipartite von Neumann entropy $\Delta S = S_j^{\text{pair}} - S_j^{\text{vac}}$, where $S_j = -\text{Tr}[\hat{\rho}_j(t)\ln\hat{\rho}_j(t)]$ with the reduced density matrix $\hat{\rho}_j(t) = \text{Tr}_{k>j}\,|\Psi(t)\rangle\langle\Psi(t)|$.

In Fig. 7(a), we show the quench to $m_f = 0$. At the collision point, the particle and antiparticle first annihilate each other, resulting in a lower local charge density compared to the quench dynamics of the pure vacuum background, with $\langle\Delta\hat{Q}\rangle < 0$. Afterward, the particle and antiparticle re-emerge due to pair production, but instead of re-emerging in their original position, the particle shows up on the right and the antiparticle shows up on the left, and in the next period they reverse in relative position again. We attribute this phenomenon to string inversion dynamics [57], where the particle and antiparticle go through each other repeatedly in the small-mass limit. In Figs. 8(c) and 8(e), we characterize the inversion by charge density imbalance between the left and right parts of the system, i.e., $I_{P,A} =$

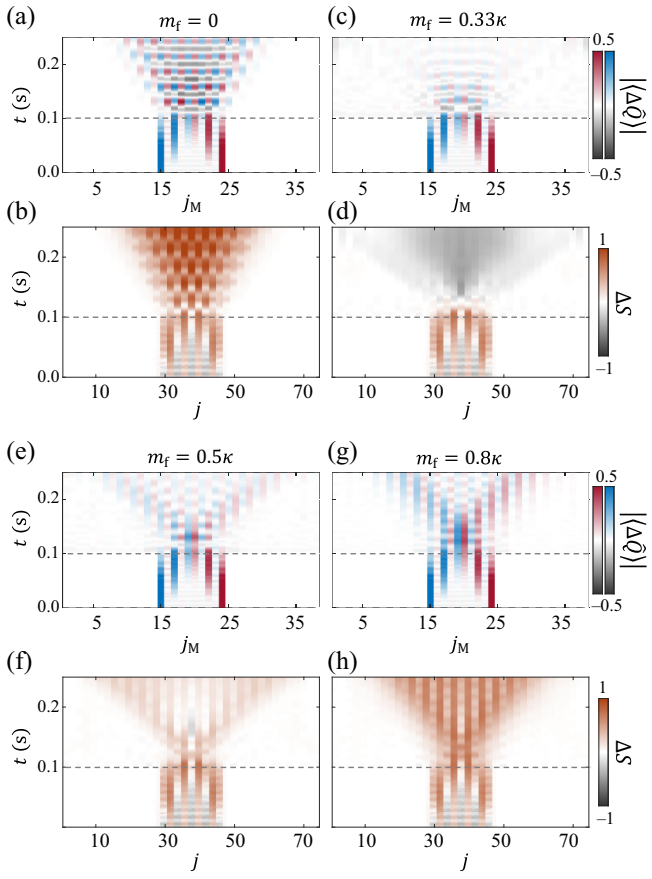

FIG. 7. Quenching mass in particle-antiparticle collisions. After the same initialization as in Fig. 6 at $m_0 = 1.5\kappa$, we quench to $m_f < m_0$ at $t = 0.1$s, with zero confining potential χ. The quenches lead to spontaneous pair production in the vacuum background. For better comparison, we subtract the evolution of the pure vacuum background from the collision dynamics for the same quenches and show their differences in particle density $\Delta\hat{Q} = \hat{Q}_{\text{pair}} - \hat{Q}_{\text{vac}}$ and entanglement entropy $\Delta S = S_{\text{pair}} - S_{\text{vac}}$. (a),(b) When quenching to $m_f = 0$, the particle and antiparticle wave packets "tunnel through" each other periodically. The colliding wave packets produce higher entropy than the pure vacuum background, which undergoes scarred dynamics that deters the growth of entanglement entropy. (c),(d) Around the critical point $m_f = m_c$, the vacuum background thermalizes, while the colliding wave packets oscillate at the collision point and exhibit slowed growth of entropy that leads to the negativity in panel (d). (e)–(h) Above the critical point, the spontaneous particle production is suppressed with increasing rest mass, and we gradually recover the low-energy elastic collision dynamics in Fig. 6.

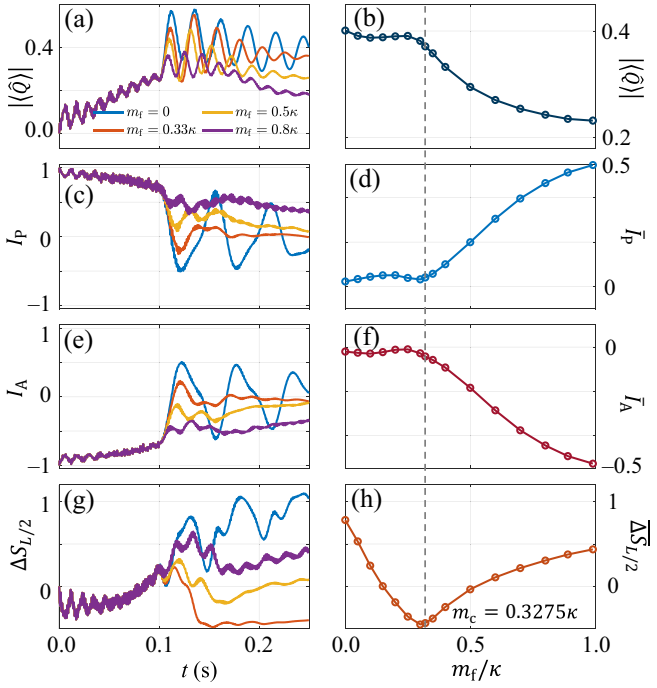

FIG. 8. Quantum criticality in the particle-antiparticle collision. (a) Real-time dynamics of the average charge density around the center ($\ell \in [16, 23]$). After the quench at $t = 0.1$ s, we observe oscillations due to pair production and annihilation. (b) Time-averaged charge density for different m_f ($t > 0.2$ s). Above m_c, pair production is exponentially suppressed. (c),(e) Density imbalance between the left and right parts of the system for the particle and antiparticle, respectively. For $m_f < m_c$, the imbalance oscillates across the zero point, indicating that the particle and antiparticle tunnel through each other by string inversion. (d),(f) Time average of (c) and (e). Above m_c, the (anti)particle is restricted to one side of the system, resulting in a nonzero imbalance. (g) Real-time dynamics of the difference in half-chain entropy $\Delta S_{j/2}$. (h) Time-averaged difference in entanglement entropy, which dips at the critical point.

$|\langle\hat{Q}\rangle|^{\text{left}}_{\text{P,A}} - |\langle\hat{Q}\rangle|^{\text{right}}_{\text{P,A}}$. The region taken into account for the imbalance of particle I_P is illustrated by the dashed blue boxes in Fig. 13(a) of Appendix D. The particle is prepared on the left with $I_P = 1$ at $t = 0$, after the quench I_P turns negative, indicating that the particle wave packet "tunneled through" the antiparticle to the right. The imbalance of antiparticle I_A mirrors that of the particle, as they reverse in position at the same frequency. In fact, the string inversion dynamics is not a unique phenomenon in lower-spin QLMs [57,58], but exists even in the full $1+1$D QED model [91], with profound connection to the string-breaking phenomenon. While we focus on the deconfined case ($\chi = 0$) here, scarring persists and can even be enhanced in the presence of confinement [92]: this behavior could also be investigated in the context of collision dynamics.

Around the critical point, the persistent string inversion is reduced and the vacuum background quickly thermalizes; see Fig. 14 in Appendix D. However, with colliding wave packets, the charge density exhibits a slower decay of oscillations; see Fig. 13(c) in Appendix D. In Fig. 8(a), we take the absolute value of the average charge density near the center where particles collide, as illustrated in the dashed black box in Fig. 13(c). We fit the oscillations of

the case at the critical point $m_f \approx m_c$ (orange) to a damped sine function and find the decay time to be $\tau \approx 0.065$ s, which is 2.5 times longer than the decay time of the vacuum background [0.026 s in Fig. 15(a) in Appendix D]. These oscillations lead to slower growth of entanglement entropy, as illustrated by the difference ΔS [Fig. 7(d)]. The colliding particle-antiparticle pair has a lower entanglement entropy than the vacuum background, indicating that they deter the onset of thermalization. Indeed, we plot the difference of the half-chain entropy $\Delta S_{L/2}$ in Fig. 8(g) and find distinct dynamics for different m_f. When we take the late-time average of them and plot with respect to the final mass, we find a dip at the critical point m_c. Microscopically, by looking at the particle density difference in Fig. 7(c), we see that the colliding wave packets oscillate at the collision point like a metastable state, compared to the fast decaying dynamics of the vacuum background; see also Fig. 14(c).

When the final mass is increased above the critical mass, we observe the suppression of string inversion, as the particle annihilation and production processes that facilitate the string inversion become energetically expensive; see Fig. 8(b). It also becomes difficult for the colliding wave packets to tunnel through each other; see Figs. 8(c) and 8(e). Towards $m_f \gg m_c$, we recover the low-energy elastic collision demonstrated in Fig. 6; see also Figs. 7(e) and 7(g). As a result, the particle and antiparticle are restricted to their initial sides, and the late-time density imbalances $\bar{I}_P$ and $\bar{I}_A$ become nonzero, while their absolute values increase with m; see Figs. 8(d) and 8(f).

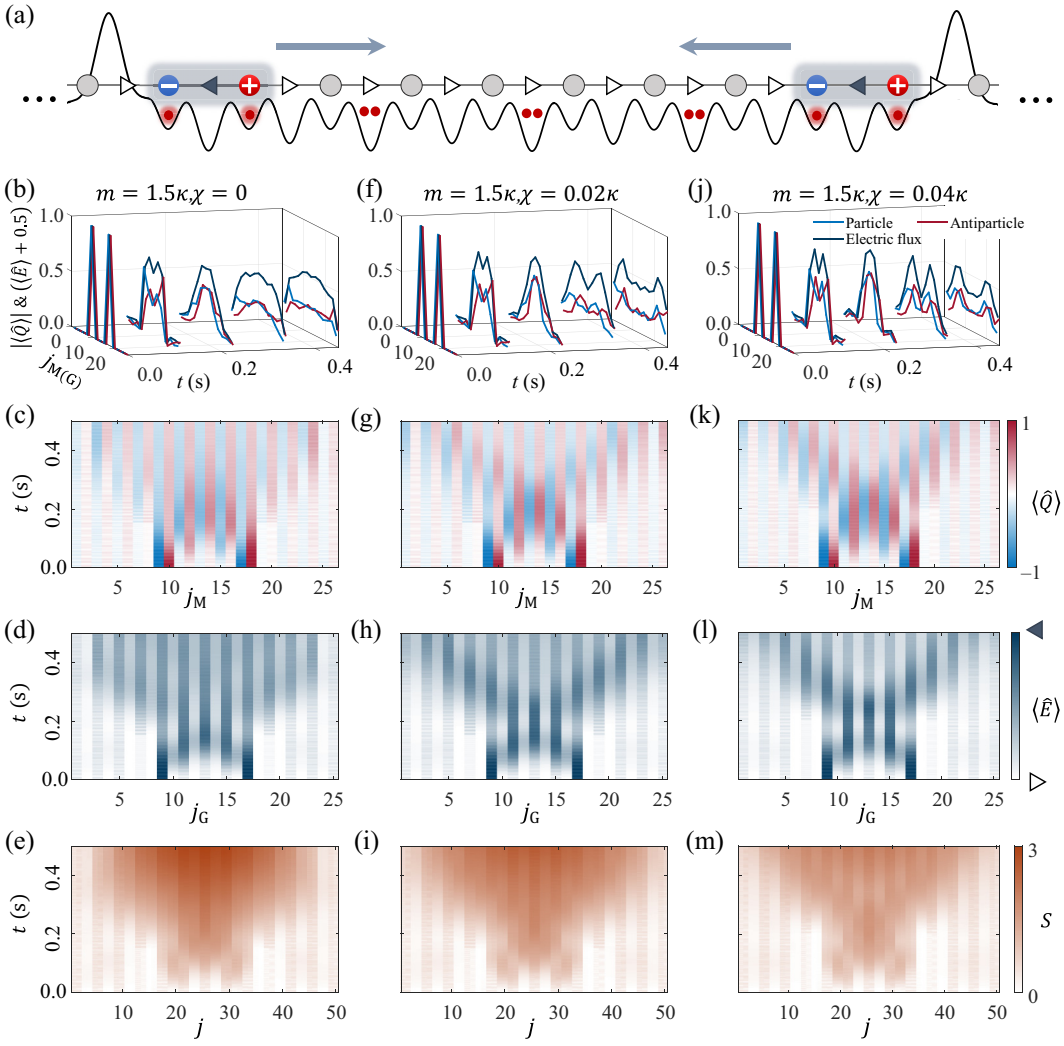

FIG. 9. Meson collisions. (a) A schematic illustration of meson collisions in the quantum simulator. (b)–(e) In the deconfined case, the particle-antiparticle pair is unstable under the collision, and both wave packets delocalize after the collision. (f)–(i) Meson scattering in the presence of a confining potential $\chi = 0.02\kappa$. (j)–(m) Meson scattering in the presence of a confining potential $\chi = 0.04\kappa$. As the confining potential χ increases, the meson wave packets become more stable, which is reflected in the postcollision entanglement entropy S as well as the electric flux $\langle\hat{E}\rangle$.

B. Meson-meson collision

We now turn to the collision of composite particles (mesons) and demonstrate how collision dynamics reveals their band structure. We focus on the large-mass case with $m = 1.5\kappa$ where spontaneous pair creation in the background is negligible. Following the protocol described in Sec. III, we initiate two meson wave packets moving towards each other; see Fig. 9(a). The barriers used to prepare the moving wave packets are removed after up to 0.2 s. Because the mesons move faster for $\chi \leq 0.02\kappa$, we remove the barriers earlier (at 0.15 s) to avoid multiple reflections on the barrier.

In the deconfined case ($\chi = 0$), shown in Figs. 9(b)–9(e), the elementary particles and antiparticles that make up the mesons scatter elastically with no string tension between one another. We find the delocalization of all wave packets and strong entropy production after the collision. The initially localized electric flux $|\blacktriangleleft\rangle$ spreads out throughout the whole system, indicating the breaking down of the particle-antiparticle pairs. We note that there is a refocus of wave packets at late times near the boundary, which is caused by reflections on the boundary.

As the confining potential is increased to $\chi = 0.02\kappa$, the mesons become more stable under the collision; see Figs. 9(f)–9(i). In this case, the particle and antiparticle wave packets remain localized after the collision, and their relative position remains unchanged since the particle and antiparticle cannot tunnel through each other in the large-mass limit. The electric fluxes $|\blacktriangleleft\rangle$ move together with the colliding particle-antiparticle pairs, and they remain largely localized after the collision. We note that the electric fluxes do leave a residue of $|\blacktriangleleft\rangle$ around the center where the mesons collide, which can be observed by the electric flux at the center, $\langle\hat{E}\rangle_{L/2,L/2+1}$. This residue is reduced as we increase χ to 0.04κ in Fig. 9(l). In Figs. 9(e), 9(i), and 9(m), we find that the entropy production decreases continuously with stronger confining potential; see also Figs. 10(c) and 10(d). Both the entropy production and the electric fluxes indicate higher meson stability with increasing confining potential χ.

To quantify this meson stability, in Fig. 10(a), we use $\langle\hat{E}\rangle_{L/2,L/2+1}$ as an observable and show its dynamics for different χ. Its real-time dynamics first grows in time and peaks around 0.2 s as the mesons collide, while after the collision it reaches different stationary values depending on the confining potential. We plot the stationary values in Fig. 10(b) and find that it plateaus around $\chi = 0.04\kappa$.

To understand this behavior, we simulate the meson collisions in the QLM and scan over m and χ. We plot the stationary values of the center electric field in a 2D dynamical phase diagram [Fig. 10(e)], where we see this plateauing behavior for different masses m. The value of χ required to reach the plateau decreases with increasing m (solid red curve).

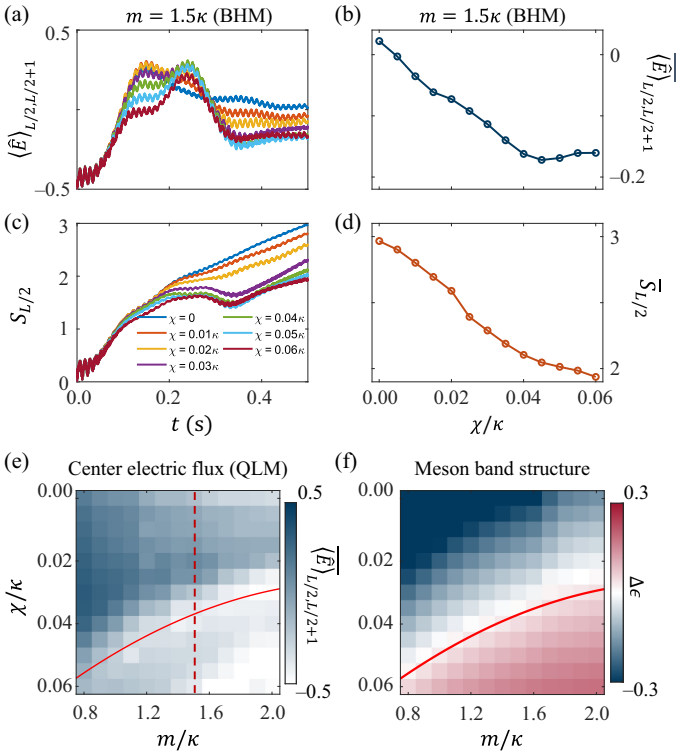

FIG. 10. Probing meson band structure in the collision dynamics. (a) Real-time dynamics of the center electric flux $\langle\hat{E}\rangle_{L/2,L/2+1}$, which relaxes to a stationary value after the collision. (b) Stationary value of $\langle\hat{E}\rangle_{L/2,L/2+1}$ in (a) extracted at late times, which decreases with χ and plateaus around $\chi = 0.04\kappa$. (c),(d) Real-time dynamics and the late-time value of the half-chain entropy $S_{L/2}$, which also decreases with χ. Both observables indicate that the meson wave packets become more stable with increasing χ. (e) A dynamical phase diagram showing the stationary value of the center electric flux $\overline{\langle\hat{E}\rangle}_{L/2,L/2+1}$ scanning over m and χ, calculated in the QLM. The red dashed line points to $m = 1.5\kappa$, which we calculated with the BHM in panel (b), where we find similar behavior of plateauing around $\chi = 0.04\kappa$. As mass m increases, the value of χ required to reach the plateau decreases (red solid curve). (f) Energy difference between the first two bands of the meson and the initial energy $\Delta\epsilon = (\epsilon_1 + \epsilon_2) - (4m + 2\chi)$.

This behavior reflects the band structure of the mesons. In the presence of a confining potential χ, the continuum of particle-antiparticle states separates into discrete bands of bound mesons, where the higher energy bands are characterized by a greater separation between the particle and antiparticle. As χ is increased, the energy spacing between these bands increases, and the higher bands become more flat due to lattice effects (see Fig. 11 and Appendix C 2). Initially, the meson wave packets occupy only the lowest band. However, during the collision, it is sometimes possible for the two mesons to scatter into a state with a lower relative momentum, where one meson is in the first

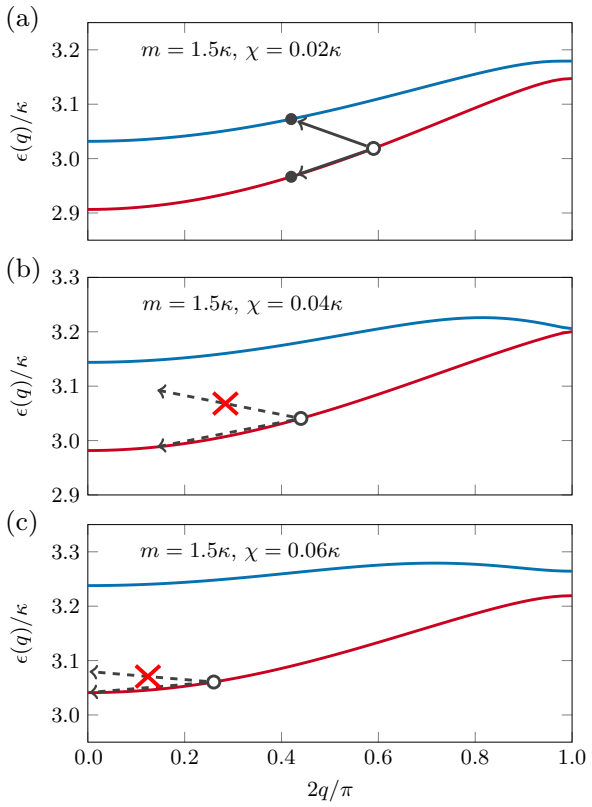

FIG. 11. Meson band structure. The excitation spectrum of the two lowest meson bands in the spin-1/2 QLM (2) with lattice spacing $a = 1$ and $m = 1.5\kappa$ for different values of the confining potential χ, calculated numerically using the matrix product state excitation ansatz (see Appendix C 2). The open circles show the initial wave-packet energies $(2m + \chi)$, created as described in Sec. III. For $\chi = 0.02\kappa$ (a), two colliding meson wave packets can exchange relative momentum, scattering into the two states shown with filled circles. For $\chi = 0.04\kappa$ (b) and 0.06κ (c), there is no way to scatter into the second band while conserving total energy.

band, and the other is in the second [Fig. 11(a)]. But, for larger χ, it is not possible to scatter into the second band while conserving total energy and momentum [Figs. 11(b) and 11(c)]. Hence, scattering into the second band should only be allowed when the sum of energies of the first two bands at the minimum $(q = 0)$ is less than the total initial energy of the two mesons $(4m + 2\chi)$. We plot the difference of these energies $\Delta\epsilon = (\epsilon_1 + \epsilon_2) - (4m + 2\chi)$ in Fig. 10(f), which shows excellent agreement with the crossover in behavior of the stationary value of the electric flux after collision shown in Fig. 10(e) (red solid curves).

V. DISCUSSION AND OUTLOOK

We presented an experimental proposal to probe particle collisions in a $1 + 1$D QED theory with a state-of-the-art cold-atom quantum simulator. Using MPS numerical calculations, we demonstrated that moving wave packets of both elementary particles and composite particles can be created with potential barriers on our quantum simulator. We studied collision dynamics both near and far from equilibrium, showing that the tunability of the quantum simulator can be used to access a wide range of energy scales. By quenching mass close to Coleman's phase transition, we observed dynamics such as string inversion and entropy production in the particle-antiparticle collisions. Meanwhile, in low-energy elastic collisions, we tuned the topological θ angle to access both confined and deconfined phases, and observed string dynamics that lead to the dynamical formation of a meson state. We further demonstrated that the meson band structure could be probed with meson-meson collisions, opening the door to understanding the structure of composite particles with quantum simulation.

Our study makes an important step towards the quantum simulation of particle collisions, which is a major objective of current working groups in the field [34,37]. As the underlying far-from-equilibrium dynamics of such processes can be highly nonperturbative, this in turn presents current quantum simulators with a true test of quantum advantage, which is a main driver of the field of quantum simulation in general.

Although we consider one particular quantum simulator implemented with cold atoms in an optical superlattice [8–10], our particle-collision scheme (using a potential barrier to generate coherent wave packets) is possible in other quantum simulation platforms, such as Rydberg-atom setups or superconducting qubits. The required investigation time can already be reached in state-of-the-art ultracold-atom quantum simulators [8,93]; nevertheless, to further minimize the effect of possible decoherence, faster dynamics can be realized by mapping the spin-1/2 QLM to the tilted BHM [50,52].

An important next step is to explore the quantum simulation of particle collisions in higher-dimensional gauge theories [94] as well as higher-spin QLMs [58,95], where confinement due to the gauge coupling term becomes important. In particular, the rich collision dynamics in the crossover from one dimension to two dimensions can be controllably studied by tuning on the coupling between initially isolated chains. Moreover, our methods also enable the exploration of dynamical string breaking with propagating charges [58,91,96].

With our studies of the band structure of both the elementary particles and composite particles, our highly controllable and versatile gauge-theory quantum simulator also presents opportunities to explore Floquet engineering methods to study particle accelerations [84], Raman-assisted tunneling [97–99], topological pumping [100–102], and to access physics of mesons in higher lattice bands.

Although our investigation here focuses on a one-dimensional gauge theory, the protocol of creating the

moving wave packets and studying collision dynamics can be generalized to various platforms and used to study particle collisions in the Bose-Hubbard and Fermi-Hubbard models, or domain wall collisions in various quantum spin models [40,103,104], and even more exotic forms of matter such as anyons [105].

ACKNOWLEDGMENTS

The authors acknowledge stimulating discussions with Monika Aidelsburger, Debasish Banerjee, Yahui Chai, Fabian Grusdt, Philipp Hauke, Karl Jansen, Wyatt Kirkby, Ian P. McCulloch, Duncan O'Dell, Bing Yang, Zhen-Sheng Yuan, and Wei-Yong Zhang. This work is supported by the Max Planck Society and the Emmy Noether Programme of the German Research Foundation (DFG) under Grant No. HA 8206/1-1. This work is part of the activities of the Quantum Computing for High-Energy Physics (QC4HEP) working group. A part of the numerical time-evolution simulations were performed on The University of Queensland's School of Mathematics and Physics Core Computing Facility `getafix`.

APPENDIX A: PERTURBATION THEORY

The Hamiltonian for the spin-1/2 QLM can be written in terms of the diagonal and off-diagonal terms with respect to the basis formed by the tensor product of $\{|\varnothing\rangle, |+\rangle\}$ for even matter sites (containing antiparticles), $\{|\varnothing\rangle, |-\rangle\}$ for odd matter sites (containing particles), and $\{|\triangleright\rangle, |\blacktriangleleft\rangle\}$ for gauge sites:

$$\hat{H}_{\text{QLM}} = \hat{H}_{\text{off-diag}} + \hat{H}_{\text{diag}} \tag{A1}$$

with

$$\hat{H}_{\text{off-diag}} = -\frac{\kappa}{2a}\sum_{\ell}(\hat{\psi}_{\ell}\hat{S}^{+}_{\ell,\ell+1}\hat{\psi}_{\ell+1} + \text{H.c.}), \tag{A2}$$

$$\hat{H}_{\text{diag}} = \frac{m}{2}\sum_{\ell}\hat{\psi}^{\dagger}_{\ell}\hat{\psi}_{\ell} - a\chi\sum_{\ell}(-1)^{\ell}\hat{S}^{z}_{\ell,\ell+1}. \tag{A3}$$

If we have some initial state containing a single particle $|i\rangle = |\ldots, \triangleright, \varnothing, \triangleright, -, \blacktriangleleft, \varnothing, \blacktriangleleft, \varnothing, \blacktriangleleft, \ldots\rangle$ and we wish to look at the state where the particle has jumped one particle site to the right, $|j\rangle = |\ldots, \triangleright, \varnothing, \triangleright, \varnothing, \triangleright, \varnothing, \triangleright, -, \blacktriangleleft, \ldots\rangle$, there is no term in $\hat{H}_{\text{off-diag}}$ that directly connects these two states. However, by second-order perturbation theory, we can determine an effective Hamiltonian coupling these two states by performing a Schrieffer-Wolff transformation on the Hamiltonian

$$\langle i|\hat{H}_{\text{eff}}|j\rangle = \delta_{ij}E_i + \frac{1}{2}\sum_{k}\left(\frac{1}{E_i - E_k} + \frac{1}{E_j - E_k}\right) \times \langle i|\hat{H}_{\text{off-diag}}|k\rangle\langle k|\hat{H}_{\text{off-diag}}|j\rangle, \tag{A4}$$

where $E_i = \langle i|\hat{H}_{\text{diag}}|i\rangle$. The only state $|k\rangle$ that will have a nonzero contribution is $|k\rangle = |\ldots, \triangleright, \varnothing, \triangleright, -, \blacktriangleleft, +, \triangleright, -, \blacktriangleleft, \ldots\rangle$, and, thus,

$$\langle i|\hat{H}_{\text{eff}}|j\rangle = \frac{1}{2}\left(\frac{1}{2m + a\chi} + \frac{1}{2m - a\chi}\right)\frac{\kappa}{2a}\frac{\kappa}{2a} = \frac{m\kappa^2}{8a^2m^2 - 2a^4\chi^2}. \tag{A5}$$

For $m \gg a\chi$, we can approximate this expression as

$$\langle i|\hat{H}_{\text{eff}}|j\rangle \approx \frac{\kappa^2}{8a^2m}. \tag{A6}$$

This will be the strength of the hopping term in the low-energy effective model (5) for particles (and antiparticles).

The approximate dispersion relation for a single particle at $\chi = 0$ is

$$\epsilon(q) = m + \frac{\kappa^2}{16a^2m}[1 - 4\cos(2aq)], \tag{A7}$$

where we include an extra shift to the energy from renormalization. The group velocity is thus

$$v_{\text{g}}(q) = \frac{\kappa^2}{2am}\sin(2aq). \tag{A8}$$

The maximum group velocity occurs at $\sin(2aq) = 1$, which will be $v_{\text{g}}^{\max} = \kappa^2/2am$. For $aq \ll 1$, we have the linear relation

$$v_{\text{g}}(q) \approx \frac{\kappa^2}{m}q. \tag{A9}$$

APPENDIX B: TIME-EVOLUTION NUMERICAL DETAILS

To access the dynamics of particle collisions in the Bose-Hubbard quantum simulator with minimum boundary effects, we perform numerical simulations of the BHM (4) with a system size of $N \gtrsim 60$. We use the time-evolving block decimation method implemented in the TenPy package [65,106] with a time step of 1×10^{-4} s $\approx 3 \times 10^{-3}J^{-1}$ and a maximum bond dimension of 3000.

For time-evolution simulations of the quantum link model (2) itself, we use the time-dependent variational principle algorithm for matrix product states [66,107,108], using a single-site evolution scheme with adaptive bond expansion, also with a time step of 1×10^{-4} s.

APPENDIX C: LOW-LYING EXCITATION SPECTRUM OF THE QUANTUM LINK MODEL

We can calculate the low-lying excitation spectrum of the QLM (2) using infinite matrix product state numerical

techniques [66]. Specifically, we use the MPS excitation ansatz [109], which is a plane-wave superposition of a local perturbation of the ground-state MPS by changing a single tensor, which is then optimized with respect to energy for a specific quasimomentum q.

1. Single-particle excitations

The single-particle excitations are topologically nontrivial excitations, in that they are domain walls between the two degenerate vacua of the QLM. (For a nonzero confining potential χ, the degeneracy between these two vacua is broken, and so this domain wall state does not have a well-defined excitation energy, so we focus only on $\chi = 0$ here.) In Fig. 12(a) we plot the dispersion relations of the lowest-energy single-particle states calculated for various m. For $m \gtrsim \kappa$, this approximately matches the sinusoidal dispersion relation (A7) of the effective model (5), but as we approach the critical point $m_c = 0.3275\kappa$, the dispersion relation changes shape and becomes more linear around $q = 0$.

2. Bound meson excitations

The meson excitations are topologically trivial excitations, that is, they are excitations on top of a single ground state. Classically, we can picture these meson excitations as being a particle-antiparticle pair with a flux string between them corresponding to the other vacuum, which we take to be the higher energy one for $\chi \neq 0$. For $\chi = 0$, the two-particle spectrum will be a continuum of scattering states, but switching to $\chi \neq 0$ will split the low-lying spectrum into discrete oscillation modes. As the potential energy of this flux string is linearly proportional to its length, the low-lying modes will approximately follow an Airy spectrum [110]. The higher energy modes will have a larger separation, and so the particle and antiparticle will localize apart from each other due to lattice effects, and the dispersion will be more flat [110].

In Fig. 11, we plot the two lowest bands of the meson excitation spectrum for $m = 1.5\kappa$ and various values of χ. We can see that, as we increase χ, the second band becomes flatter and more well separated from the first.

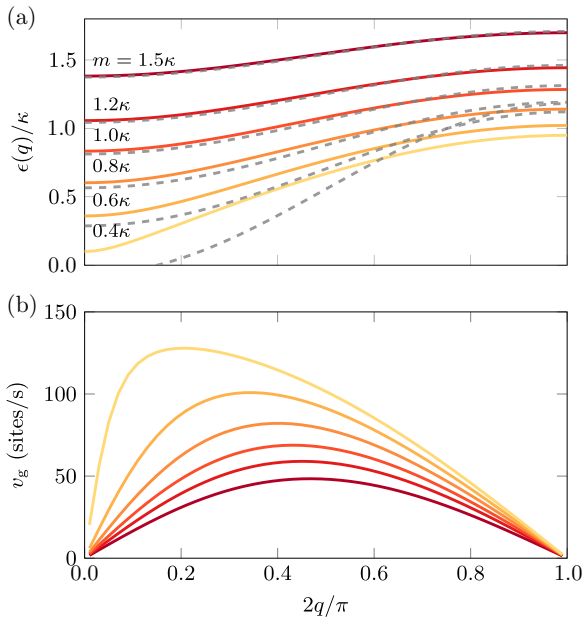

FIG. 12. Single-particle spectra. (a) The single-particle excitation spectrum of the spin-1/2 QLM (2) with lattice spacing $a = 1$ and confining potential $\chi = 0$, scanning across various masses, approaching the critical point $m_c = 0.3275\kappa$ from above, calculated numerically using the matrix product state excitation ansatz. For large m, this dispersion relation approximately matches the sinusoidal dispersion relation (A7) of the effective model (5) (shown as the dashed gray curves on top of the data). (b) The corresponding group velocities.

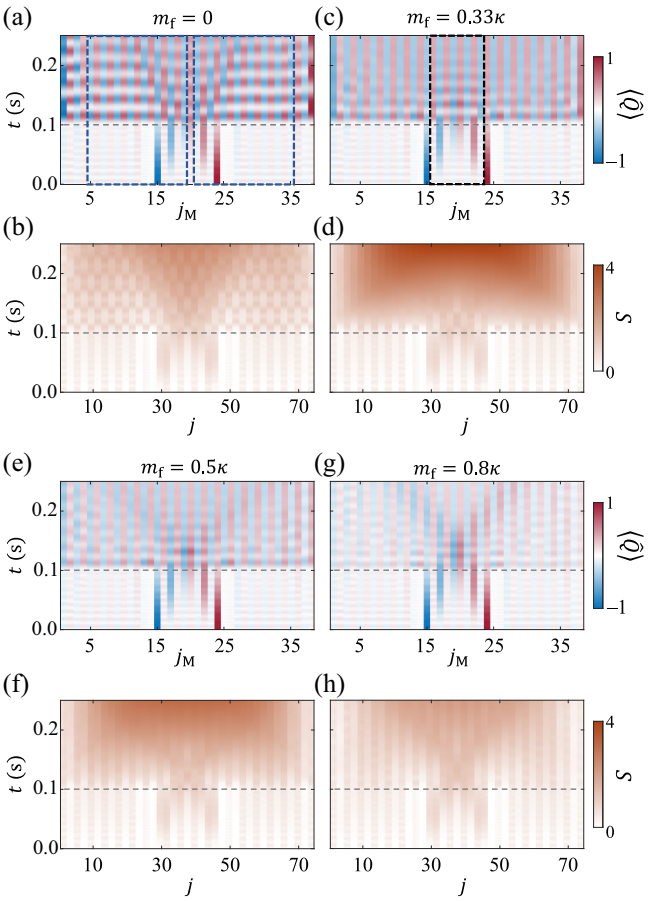

FIG. 13. Particle-antiparticle collision in the wake of a mass quench. (a),(b) Quenching mass to $m_f = 0$ at 0.1 s. The dashed blue boxes in (a) show the left and right regions used to calculate the particle imbalances I_P in Fig. 8(c). (c),(d) A quench to the critical point $m_f \approx m_c$. The dashed black box in (c) shows the region used to calculate the average charge density in Fig. 8(a). (e)–(h) For m_f above the critical point, the low-energy elastic collision dynamics in Fig. 6 is gradually recovered.

APPENDIX D: DETAILS ON QUENCHES IN PARTICLE-ANTIPARTICLE COLLISIONS

In Sec. IV A we accessed dynamics of various energy scales by quenching the rest mass to different m_f. Furthermore, for a better comparison, we subtracted the dynamics of the background vacuum from the colliding wave packets. Here in Fig. 13, we show the dynamics of the collision without this subtraction. With $m_f \gtrsim 0.8\kappa$ [Fig. 13(g)], the phenomenon is close to Fig. 7(g), as pair creation in the background is suppressed; see also Fig. 14(g). When m_f is reduced, the signal of initial wave packets is covered by the particles produced in the background; see Fig. 13(e). However, at $m_f = 0$, the background undergoes scarred dynamics [Fig. 14(a)], and the propagation of wave packets creates a phase shift with light-cone-shaped spread, similar to the observation in Ref. [57]. Moreover, around the critical point, we observe longer-lasting oscillations of the charge density at the collision point [Fig. 13(c)] compared to the background [Fig. 14(c)]. This comparison is even more clear when we compare the evolution of the average charge density around the center (orange curves for $m_f \approx m_c$) in Figs. 8(a) and 15(a). We extract the decay time of their oscillations by fitting to a damped sine function in Fig. 15(a), where the decay time of the orange curve is found to be $\tau \approx 0.026$ s, which is 2.5 times faster compared to $\tau \approx 0.065$ s in Fig. 8(a). These oscillations lead to a slower thermalization, which is reflected in the half-chain entropy difference between the background [Fig. 15(c)] and the colliding wave packets [Fig. 15(d)], with their difference shown in Fig. 8(g).

In Fig. 15(b) we observe that, for the vacuum background, the imbalance in the particle density between the left and right parts of the system shows no significant change over time after the quench, since no initial wave packets are present in the system.

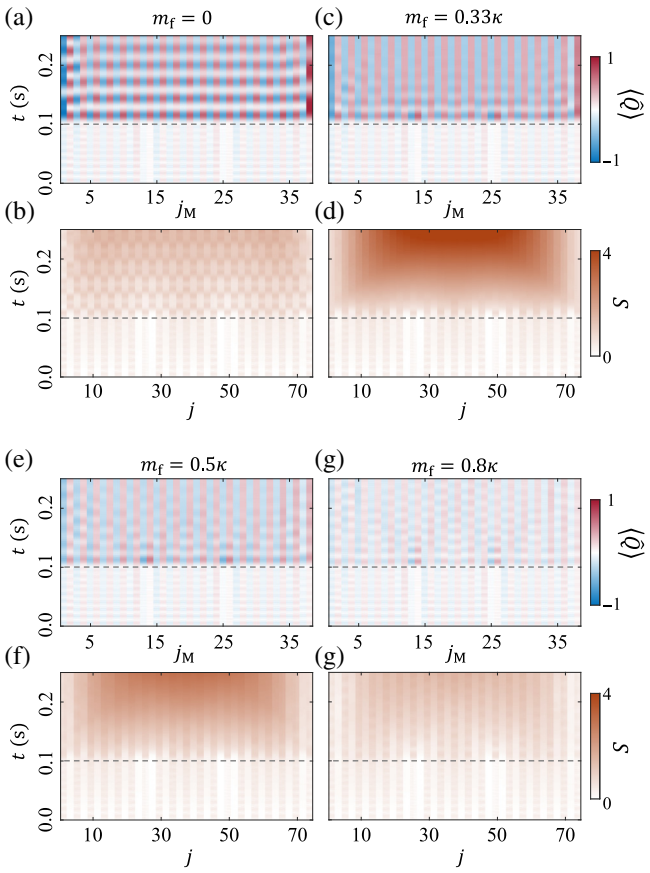

FIG. 14. Evolution of the vacuum background in the wake of a mass quench. (a),(b) The background exhibits quantum many-body scarring at $m_f = 0$, with slowed growth of entanglement entropy. (c),(d) Around the critical point m_c, the vacuum background quickly thermalizes. (e)–(h) Above the critical point, spontaneous pair production in the vacuum background is suppressed with increasing mass.

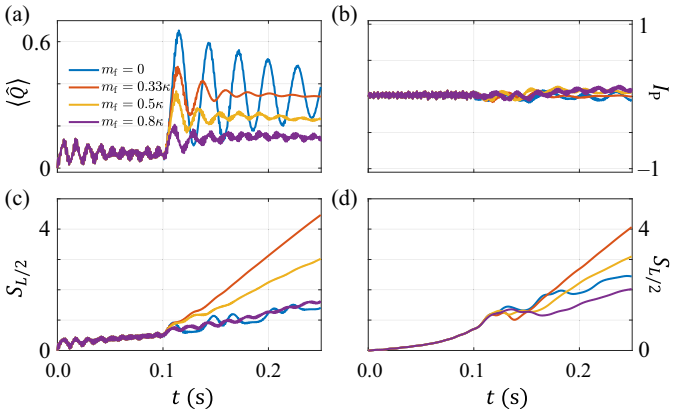

FIG. 15. (a) Dynamics of the average charge density of the vacuum background when quenched to m_f at 0.1 s for the same sites as in Fig. 8(a). (b) Left-right imbalance of the vacuum background, which shows no significant change. (c),(d) Half-chain entropy of the vacuum background and the colliding wave packets for quenches to various m_f, respectively. Around the critical point (orange curves), the entropy of colliding wave packets exhibits an initial dip before the linear rise, which leads to lower entanglement entropy throughout the evolution times.

[1] R. K. Ellis, W. J. Stirling, and B. R. Webber, *QCD and Collider Physics*, Cambridge Monographs on Particle Physics, Nuclear Physics and Cosmology (Cambridge University Press, 2003). https://books.google.de/books?id=TqrPVoS6s0UC.

[2] ATLAS Collaboration, Observation of a new particle in the search for the Standard Model Higgs boson with the ATLAS detector at the LHC, Physics Letters B **716**, 1 (2012).

[3] CMS Collaboration, Observation of a new boson at a mass of 125 GeV with the CMS experiment at the LHC, Phys. Lett. B **716**, 30 (2012).

[4] K. Adcox, S. S. Adler, S. Afanasiev, C. Aidala, N. N. Ajitanand, Y. Akiba, A. Al-Jamel, J. Alexander, R. Amirikas, and K. Aoki, *et al.*, Formation of dense partonic matter in relativistic nucleus–nucleus collisions at RHIC: Experimental evaluation by the PHENIX Collaboration, Nucl. Phys. A **757**, 184 (2005).

[5] B. B. Back, M. D. Baker, M. Ballintijn, D. S. Barton, B. Becker, R. R. Betts, A. A. Bickley, R. Bindel, A. Budzanowski, W. Busza, *et al.*, The PHOBOS perspective on discoveries at RHIC, Nucl. Phys. A **757**, 28 (2005).

[6] I. Arsene, I. G. Bearden, D. Beavis, C. Besliu, B. Budick, H. Bøggild, C. Chasman, C. H. Christensen, P. Christiansen, J. Cibor, *et al.*, Quark–gluon plasma and color glass condensate at RHIC? The perspective from the BRAHMS experiment, Nucl. Phys. A **757**, 1 (2005).

[7] M. Benedikt and F. Zimmermann, https://cerncourier.com/a/the-future-circular-collider-study/ (2014).

[8] Bing Yang, Hui Sun, Robert Ott, Han-Yi Wang, Torsten V. Zache, Jad C. Halimeh, Zhen-Sheng Yuan, Philipp Hauke, and Jian-Wei Pan, Observation of gauge invariance in a 71-site Bose–Hubbard quantum simulator, Nature **587**, 392 (2020).

[9] Zhao-Yu Zhou, Guo-Xian Su, Jad C. Halimeh, Robert Ott, Hui Sun, Philipp Hauke, Bing Yang, Zhen-Sheng Yuan, Jürgen Berges, and Jian-Wei Pan, Thermalization dynamics of a gauge theory on a quantum simulator, Science **377**, 311 (2022).

[10] Jad C. Halimeh, Ian P. McCulloch, Bing Yang, and Philipp Hauke, Tuning the topological θ-angle in cold-atom quantum simulators of gauge theories, PRX Quantum **3**, 040316 (2022).

[11] E. Rico, T. Pichler, M. Dalmonte, P. Zoller, and S. Montangero, Tensor networks for lattice gauge theories and atomic quantum simulation, Phys. Rev. Lett. **112**, 201601 (2014).

[12] Torbjörn Sjöstrand, High-energy-physics event generation with PYTHIA 5.7 and JETSET 7.4, Comput. Phys. Commun. **82**, 74 (1994).

[13] M. E. Peskin and D. V. Schroeder, *An Introduction To Quantum Field Theory* (CRC Press, Boca Raton, Florida, United States, 2018). https://books.google.de/books?id=9EpnDwAAQBAJ.

[14] John C. Collins, Davison E. Soper, and George Sterman, in *Perturbative QCD* (World Scientific Publishing, Singapore, 1989), Vol. 5, p. 1.

[15] François Gelis and Naoto Tanji, Schwinger mechanism revisited, Prog. Part. Nucl. Phys. **87**, 1 (2016).

[16] Jürgen Berges, Michal P. Heller, Aleksas Mazeliauskas, and Raju Venugopalan, QCD thermalization: Ab initio approaches and interdisciplinary connections, Rev. Mod. Phys. **93**, 035003 (2021).

[17] Steven R. White and Adrian E. Feiguin, Real-time evolution using the density matrix renormalization group, Phys. Rev. Lett. **93**, 076401 (2004).

[18] U. Schollwöck, The density-matrix renormalization group, Rev. Mod. Phys. **77**, 259 (2005).

[19] Ulrich Schollwöck, The density-matrix renormalization group in the age of matrix product states, Ann. Phys. **326**, 96 (2011), January 2011 Special Issue,

[20] Sebastian Paeckel, Thomas Köhler, Andreas Swoboda, Salvatore R. Manmana, Ulrich Schollwöck, and Claudius Hubig, Time-evolution methods for matrix-product states, Ann. Phys. **411**, 167998 (2019).

[21] B. Andersson, G. Gustafson, G. Ingelman, and T. Sjöstrand, Parton fragmentation and string dynamics, Phys. Rep. **97**, 31 (1983).

[22] Richard P. Feynman, Simulating physics with computers, Int. J. Theor. Phys. **21**, 467 (1982).

[23] Seth Lloyd, Universal quantum simulators, Science **273**, 1073 (1996).

[24] Immanuel Bloch, Jean Dalibard, and Wilhelm Zwerger, Many-body physics with ultracold gases, Rev. Mod. Phys. **80**, 885 (2008).

[25] Philipp Hauke, Fernando M. Cucchietti, Luca Tagliacozzo, Ivan Deutsch, and Maciej Lewenstein, Can one trust quantum simulators?, Rep. Prog. Phys. **75**, 082401 (2012).

[26] I. M. Georgescu, S. Ashhab, and Franco Nori, Quantum simulation, Rev. Mod. Phys. **86**, 153 (2014).

[27] M. Dalmonte and S. Montangero, Lattice gauge theory simulations in the quantum information era, Contemp. Phys. **57**, 388 (2016).

[28] Mari Carmen Bañuls, *et al.*, Simulating lattice gauge theories within quantum technologies, Eur. Phys. J. D **74**, 165 (2020).

[29] Erez Zohar, J. Ignacio Cirac, and Benni Reznik, Quantum simulations of lattice gauge theories using ultracold atoms in optical lattices, Rep. Prog. Phys. **79**, 014401 (2015).

[30] Yuri Alexeev, *et al.*, Quantum computer systems for scientific discovery, PRX Quantum **2**, 017001 (2021).

[31] Monika Aidelsburger, *et al.*, Cold atoms meet lattice gauge theory, Phys. Eng. Sci. **380**, 20210064 (2022).

[32] Erez Zohar, Quantum simulation of lattice gauge theories in more than one space dimension: Requirements, challenges and methods, Philos. Trans. R. Soc. A: Math. Phys. Eng. Sci. **380**, 20210069 (2022).

[33] Natalie Klco, Alessandro Roggero, and Martin J. Savage, Standard model physics and the digital quantum revolution: Thoughts about the interface, Rep. Prog. Phys. **85**, 064301 (2022).

[34] Christian W. Bauer, *et al.*, Quantum simulation for high-energy physics, PRX Quantum **4**, 027001 (2023).

[35] Christian W. Bauer, Zohreh Davoudi, Natalie Klco, and Martin J. Savage, Quantum simulation of fundamental particles and forces, Nat. Rev. Phys. **5**, 420 (2023).

[36] Lena Funcke, Tobias Hartung, Karl Jansen, and Stefan Kühn, Review on quantum computing for lattice field theory, arXiv:2302.00467.

[37] Alberto Di Meglio, *et al.*, Quantum computing for high-energy physics: State of the art and challenges. Summary of the QC4HEP working group, PRX Quantum **5**, 037001 (2024).

[38] Jad C. Halimeh, Monika Aidelsburger, Fabian Grusdt, Philipp Hauke, and Bing Yang, Cold-atom quantum simulators of gauge theories, arXiv:2310.12201.

[39] Esteban A. Martinez, Christine A. Muschik, Philipp Schindler, Daniel Nigg, Alexander Erhard, Markus Heyl, Philipp Hauke, Marcello Dalmonte, Thomas Monz, Peter Zoller, and Rainer Blatt, Real-time dynamics of lattice gauge theories with a few-qubit quantum computer, Nature **534**, 516 (2016).

[40] Hannes Bernien, Sylvain Schwartz, Alexander Keesling, Harry Levine, Ahmed Omran, Hannes Pichler, Soonwon Choi, Alexander S. Zibrov, Manuel Endres, Markus Greiner, Vladan Vuletić, and Mikhail D. Lukin, Probing many-body dynamics on a 51-atom quantum simulator, Nature **551**, 579 (2017).

[41] Han-Ning Dai, Bing Yang, Andreas Reingruber, Hui Sun, Xiao-Fan Xu, Yu-Ao Chen, Zhen-Sheng Yuan, and Jian-Wei Pan, Four-body ring-exchange interactions and anyonic statistics within a minimal toric-code Hamiltonian, Nat. Phys. **13**, 1195 (2017).

[42] N. Klco, E. F. Dumitrescu, A. J. McCaskey, T. D. Morris, R. C. Pooser, M. Sanz, E. Solano, P. Lougovski, and M. J. Savage, Quantum-classical computation of Schwinger model dynamics using quantum computers, Phys. Rev. A **98**, 032331 (2018).

[43] Frederik Görg, Kilian Sandholzer, Joaquín Minguzzi, Rémi Desbuquois, Michael Messer, and Tilman Esslinger, Realization of density-dependent Peierls phases to engineer quantized gauge fields coupled to ultracold matter, Nat. Phys. **15**, 1161 (2019).

[44] Christian Schweizer, Fabian Grusdt, Moritz Berngruber, Luca Barbiero, Eugene Demler, Nathan Goldman, Immanuel Bloch, and Monika Aidelsburger, Floquet approach to $\mathbb{Z}2$ lattice gauge theories with ultracold atoms in optical lattices, Nat. Phys. **15**, 1168 (2019).

[45] Alexander Mil, Torsten V. Zache, Apoorva Hegde, Andy Xia, Rohit P. Bhatt, Markus K. Oberthaler, Philipp Hauke, Jürgen Berges, and Fred Jendrzejewski, A scalable realization of local U(1) gauge invariance in cold atomic mixtures, Science **367**, 1128 (2020).

[46] Zhan Wang, Zi-Yong Ge, Zhongcheng Xiang, Xiaohui Song, Rui-Zhen Huang, Pengtao Song, Xue-Yi Guo, Luhong Su, Kai Xu, Dongning Zheng, and Heng Fan, Observation of emergent F_2 gauge invariance in a superconducting circuit, Phys. Rev. Res. **4**, L022060 (2022).

[47] Julius Mildenberger, Wojciech Mruczkiewicz, Jad C. Halimeh, Zhang Jiang, and Philipp Hauke, Probing confinement in a $\mathbb{Z}_2$ lattice gauge theory on a quantum computer, arXiv:2203.08905.

[48] Roland C. Farrell, Marc Illa, Anthony N. Ciavarella, and Martin J. Savage, Scalable circuits for preparing ground states on digital quantum computers: The Schwinger model vacuum on 100 qubits, PRX Quantum **5**, 020315 (2024).

[49] Takis Angelides, Pranay Naredi, Arianna Crippa, Karl Jansen, Stefan Kühn, Ivano Tavernelli, and Derek S. Wang, First-order phase transition of the Schwinger model with a quantum computer, arXiv:2312.12831.

[50] Guo-Xian Su, Hui Sun, Ana Hudomal, Jean-Yves Desaules, Zhao-Yu Zhou, Bing Yang, Jad C. Halimeh, Zhen-Sheng Yuan, Zlatko Papić, and Jian-Wei Pan, Observation of many-body scarring in a Bose-Hubbard quantum simulator, Phys. Rev. Res. **5**, 023010 (2023).

[51] Han-Yi Wang, Wei-Yong Zhang, Zhiyuan Yao, Ying Liu, Zi-Hang Zhu, Yong-Guang Zheng, Xuan-Kai Wang, Hui Zhai, Zhen-Sheng Yuan, and Jian-Wei Pan, Interrelated thermalization and quantum criticality in a lattice gauge simulator, Phys. Rev. Lett. **131**, 050401 (2023).

[52] Wei-Yong Zhang, Ying Liu, Yanting Cheng, Ming-Gen He, Han-Yi Wang, Tian-Yi Wang, Zi-Hang Zhu, Guo-Xian Su, Zhao-Yu Zhou, Yong-Guang Zheng, Hui Sun, Bing Yang, Philipp Hauke, Wei Zheng, Jad C. Halimeh, Zhen-Sheng Yuan, and Jian-Wei Pan, Observation of microscopic confinement dynamics by a tunable topological θ-angle, arXiv:2306.11794.

[53] Jad C. Halimeh and Philipp Hauke, Reliability of lattice gauge theories, Phys. Rev. Lett. **125**, 030503 (2020).

[54] Jad C. Halimeh, Haifeng Lang, Julius Mildenberger, Zhang Jiang, and Philipp Hauke, Gauge-symmetry protection using single-body terms, PRX Quantum **2**, 040311 (2021).

[55] Maarten Van Damme, Haifeng Lang, Philipp Hauke, and Jad C. Halimeh, Reliability of lattice gauge theories in the thermodynamic limit, Phys. Rev. B **107**, 035153 (2023).

[56] Jad C. Halimeh and Philipp Hauke, Stabilizing gauge theories in quantum simulators: A brief review, arXiv:2204.13709.

[57] Federica M. Surace, Paolo P. Mazza, Giuliano Giudici, Alessio Lerose, Andrea Gambassi, and Marcello Dalmonte, Lattice gauge theories and string dynamics in Rydberg atom quantum simulators, Phys. Rev. X **10**, 021041 (2020).

[58] T. Pichler, M. Dalmonte, E. Rico, P. Zoller, and S. Montangero, Real-time dynamics in U(1) lattice gauge theories with tensor networks, Phys. Rev. X **6**, 011023 (2016).

[59] Marco Rigobello, Simone Notarnicola, Giuseppe Magnifico, and Simone Montangero, Entanglement generation in (1+1)D QED scattering processes, Phys. Rev. D **104**, 114501 (2021).

[60] Federica Maria Surace and Alessio Lerose, Scattering of mesons in quantum simulators, New J. Phys. **23**, 062001 (2021).

[61] Yahui Chai, Arianna Crippa, Karl Jansen, Stefan Kühn, Vincent R. Pascuzzi, Francesco Tacchino, and Ivano Tavernelli, Entanglement production from scattering of fermionic wave packets: A quantum computing approach, arXiv:2312.02272.

[62] Ron Belyansky, Seth Whitsitt, Niklas Mueller, Ali Fahimniya, Elizabeth R. Bennewitz, Zohreh Davoudi, and Alexey V. Gorshkov, High-energy collision of quarks and mesons in the Schwinger model: from tensor networks to circuit QED, Phys. Rev. Lett. **132**, 091903 (2024).

[63] Joseph Vovrosh, Rick Mukherjee, Alvise Bastianello, and Johannes Knolle, Dynamical Hadron formation in long-range interacting quantum spin chains, PRX Quantum **3**, 040309 (2022).

[64] Ashley Milsted, Junyu Liu, John Preskill, and Guifre Vidal, Collisions of false-vacuum bubble walls in a quantum spin chain, PRX Quantum **3**, 1 (2022).

[65] Johannes Hauschild and Frank Pollmann, Efficient numerical simulations with tensor networks: Tensor Network Python (TeNPy), SciPost Phys. Lect. Notes **5**, 5 (2018).

[66] Ian P. McCulloch, Matrix product toolkit, https://github.com/mptoolkit.

[67] John Kogut and Leonard Susskind, Hamiltonian formulation of Wilson's lattice gauge theories, Phys. Rev. D **11**, 395 (1975).

[68] Leonard Susskind, Lattice fermions, Phys. Rev. D **16**, 3031 (1977).
[69] Sidney Coleman, R. Jackiw, and Leonard Susskind, Charge shielding and quark confinement in the massive Schwinger model, Ann. Phys. **93**, 267 (1975).
[70] S. Chandrasekharan and U.-J. Wiese, Quantum link models: A discrete approach to gauge theories, Nucl. Phys. B **492**, 455 (1997).
[71] U.-J. Wiese, Ultracold quantum gases and lattice systems: Quantum simulation of lattice gauge theories, Ann. Phys. **525**, 777 (2013).
[72] V. Kasper, F. Hebenstreit, F. Jendrzejewski, M. K. Oberthaler, and J. Berges, Implementing quantum electrodynamics with ultracold atomic systems, New J. Phys. **19**, 023030 (2017).
[73] Dayou Yang, Gouri Shankar Giri, Michael Johanning, Christof Wunderlich, Peter Zoller, and Philipp Hauke, Analog quantum simulation of $(1+1)$-dimensional lattice QED with trapped ions, Phys. Rev. A **94**, 052321 (2016).
[74] Boye Buyens, Simone Montangero, Jutho Haegeman, Frank Verstraete, and Karel Van Acoleyen, Finite-representation approximation of lattice gauge theories at the continuum limit with tensor networks, Phys. Rev. D **95**, 094509 (2017).
[75] Mari Carmen Bañuls and Krzysztof Cichy, Review on novel methods for lattice gauge theories, Rep. Prog. Phys. **83**, 024401 (2020).
[76] Torsten V. Zache, Maarten Van Damme, Jad C. Halimeh, Philipp Hauke, and Debasish Banerjee, Toward the continuum limit of a $(1+1)$D quantum link Schwinger model, Phys. Rev. D **106**, L091502 (2022).
[77] Jad C. Halimeh, Maarten Van Damme, Torsten V. Zache, Debasish Banerjee, and Philipp Hauke, Achieving the quantum field theory limit in far-from-equilibrium quantum link models, Quantum **6**, 878 (2022).
[78] Yanting Cheng, Shang Liu, Wei Zheng, Pengfei Zhang, and Hui Zhai, Tunable confinement-deconfinement transition in an ultracold-atom quantum simulator, PRX Quantum **3**, 040317 (2022).
[79] Sidney Coleman, More about the massive Schwinger model, Ann. Phys. **101**, 239 (1976).
[80] Kenneth G. Wilson, Confinement of quarks, Phys. Rev. D **10**, 2445 (1974).
[81] Jad C. Halimeh, Robert Ott, Ian P. McCulloch, Bing Yang, and Philipp Hauke, Robustness of gauge-invariant dynamics against defects in ultracold-atom gauge theories, Phys. Rev. Res. **2**, 033361 (2020).
[82] S. Weinberg, *The Quantum Theory of Fields, Vol. 2: Modern Applications* (Cambridge University Press, Cambridge, United Kingdom, 1995). https://books.google.de/books?id=doeDB3_WLvwC.
[83] Philipp M. Preiss, Ruichao Ma, M. Eric Tai, Alexander Lukin, Matthew Rispoli, Philip Zupancic, Yoav Lahini, Rajibul Islam, and Markus Greiner, Strongly correlated quantum walks in optical lattices, Science **347**, 1229 (2015).
[84] T. Hartmann, F. Keck, H. J. Korsch, and S. Mossmann, Dynamics of Bloch oscillations, New. J. Phys. **6**, 2 (2004).
[85] Christof Weitenberg, Manuel Endres, Jacob F. Sherson, Marc Cheneau, Peter Schausz, Takeshi Fukuhara, Immanuel Bloch, and Stefan Kuhr, Single-spin addressing in an atomic Mott insulator, Nature **471**, 319 (2011).
[86] Rajibul Islam, Ruichao Ma, Philipp M. Preiss, M. Eric Tai, Alexander Lukin, Matthew Rispoli, and Markus Greiner, Measuring entanglement entropy in a quantum many-body system, Nature **528**, 77 (2015).
[87] Bing Yang, Hui Sun, Chun-Jiong Huang, Han-Yi Wang, Youjin Deng, Han-Ning Dai, Zhen-Sheng Yuan, and Jian-Wei Pan, Cooling and entangling ultracold atoms in optical lattices, Science **369**, 550 (2020).
[88] Zhiyuan Yao, Lei Pan, Shang Liu, and Hui Zhai, Quantum many-body scars and quantum criticality, Phys. Rev. B **105**, 125123 (2022).
[89] C. J. Turner, A. A. Michailidis, D. A. Abanin, M. Serbyn, and Z. Papić, Weak ergodicity breaking from quantum many-body scars, Nat. Phys. **14**, 745 (2018).
[90] C. J. Turner, A. A. Michailidis, D. A. Abanin, M. Serbyn, and Z. Papić, Quantum scarred eigenstates in a Rydberg atom chain: Entanglement, breakdown of thermalization, and stability to perturbations, Phys. Rev. B **98**, 155134 (2018).
[91] F. Hebenstreit, J. Berges, and D. Gelfand, Real-time dynamics of string breaking, Phys. Rev. Lett. **111**, 201601 (2013).
[92] Jean Yves Desaules, Guo Xian Su, Ian P. McCulloch, Bing Yang, Zlatko Papić, and Jad C. Halimeh, Ergodicity breaking under confinement in cold-atom quantum simulators, Quantum **8**, 1274 (2024).
[93] Julian F. Wienand, Simon Karch, Alexander Impertro, Christian Schweizer, Ewan McCulloch, Romain Vasseur, Sarang Gopalakrishnan, Monika Aidelsburger, and Immanuel Bloch, Emergence of fluctuating hydrodynamics in chaotic quantum systems, arXiv:2306.11457.
[94] Jesse Osborne, Ian P. McCulloch, Bing Yang, Philipp Hauke, and Jad C. Halimeh, Large-scale $2+1$D U(1) gauge theory with dynamical matter in a cold-atom quantum simulator, arXiv:2211.01380.
[95] Jesse Osborne, Bing Yang, Ian P. McCulloch, Philipp Hauke, and Jad C. Halimeh, Spin-S U(1) quantum link models with dynamical matter on a quantum simulator, arXiv:2305.06368.
[96] F. Hebenstreit, J. Berges, and D. Gelfand, Simulating fermion production in $1+1$ dimensional QED, Phys. Rev. D **87**, 105006 (2013).
[97] André Eckardt, Colloquium: Atomic quantum gases in periodically driven optical lattices, Rev. Mod. Phys. **89**, 011004 (2017).
[98] M. Aidelsburger, M. Atala, M. Lohse, J. T. Barreiro, B. Paredes, and I. Bloch, Realization of the Hofstadter Hamiltonian with ultracold atoms in optical lattices, Phys. Rev. Lett. **111**, 185301 (2013).
[99] Julian Léonard, Sooshin Kim, Joyce Kwan, Perrin Segura, Fabian Grusdt, Cécile Repellin, Nathan Goldman, and Markus Greiner, Realization of a fractional quantum Hall state with ultracold atoms, Nature **619**, 495 (2023).
[100] Michael Lohse, Christian Schweizer, Oded Zilberberg, Monika Aidelsburger, and Immanuel Bloch, A Thouless quantum pump with ultracold bosonic

atoms in an optical superlattice, Nat. Phys. **12**, 350 (2016).

[101] Joaquín Minguzzi, Zijie Zhu, Kilian Sandholzer, Anne-Sophie Walter, Konrad Viebahn, and Tilman Esslinger, Topological pumping in a Floquet-Bloch band, Phys. Rev. Lett. **129**, 53201 (2022).

[102] Anne-Sophie Walter, Zijie Zhu, Marius Gächter, Joaquín Minguzzi, Stephan Roschinski, Kilian Sandholzer, Konrad Viebahn, and Tilman Esslinger, Quantization and its breakdown in a Hubbard–Thouless pump, Nat. Phys. **19**, 1471 (2023).

[103] David Wei, Antonio Rubio-Abadal, Bingtian Ye, Francisco Machado, Jack Kemp, Kritsana Srakaew, Simon Hollerith, Jun Rui, Sarang Gopalakrishnan, Norman Y. Yao, Immanuel Bloch, and Johannes Zeiher, Quantum gas microscopy of Kardar-Parisi-Zhang superdiffusion, Science **376**, 716 (2022).

[104] W. L. Tan, P. Becker, F. Liu, G. Pagano, K. S. Collins, A. De, L. Feng, H. B. Kaplan, A. Kyprianidis, R. Lundgren, W. Morong, S. Whitsitt, A. V. Gorshkov, and C. Monroe, Domain-wall confinement and dynamics in a quantum simulator, Nat. Phys. **17**, 742 (2021).

[105] Joyce Kwan, Perrin Segura, Yanfei Li, Sooshin Kim, Alexey V. Gorshkov, Brice Bakkali-hassani, and Markus Greiner, Realization of 1D anyons with arbitrary statistical phase, arXiv:2306.01737v1.

[106] Guifré Vidal, Efficient simulation of one-dimensional quantum many-body systems, Phys. Rev. Lett. **93**, 040502 (2004).

[107] Jutho Haegeman, J. Ignacio Cirac, Tobias J. Osborne, Iztok Pižorn, Henri Verschelde, and Frank Verstraete, Time-dependent variational principle for quantum lattices, Phys. Rev. Lett. **107**, 070601 (2011).

[108] Jutho Haegeman, Christian Lubich, Ivan Oseledets, Bart Vandereycken, and Frank Verstraete, Unifying time evolution and optimization with matrix product states, Phys. Rev. B **94**, 165116 (2016).

[109] Jutho Haegeman, Bogdan Pirvu, David J. Weir, J. Ignacio Cirac, Tobias J. Osborne, Henri Verschelde, and Frank Verstraete, Variational matrix product ansatz for dispersion relations, Phys. Rev. B **85**, 100408 (2012).

[110] S. B. Rutkevich, Energy spectrum of bound-spinons in the quantum Ising spin-chain ferromagnet, J. Stat. Phys. **131**, 917 (2008).